



**HAL**  
open science

## Modeling of Young's modulus variations with temperature of Ni and oxidized Ni using a magneto-mechanical approach

Olivier Hubert, Xavier Milhet, Pascal Gadaud, Mathieu Tatat, Pierre-Olivier Renault, Christophe Coupeau

### ► To cite this version:

Olivier Hubert, Xavier Milhet, Pascal Gadaud, Mathieu Tatat, Pierre-Olivier Renault, et al.. Modeling of Young's modulus variations with temperature of Ni and oxidized Ni using a magneto-mechanical approach. *Materials Science and Engineering: A*, 2015, 633, pp.76-91. 10.1016/j.msea.2015.03.014 . hal-01530469

**HAL Id: hal-01530469**

**<https://hal.science/hal-01530469>**

Submitted on 31 May 2017

**HAL** is a multi-disciplinary open access archive for the deposit and dissemination of scientific research documents, whether they are published or not. The documents may come from teaching and research institutions in France or abroad, or from public or private research centers.

L'archive ouverte pluridisciplinaire **HAL**, est destinée au dépôt et à la diffusion de documents scientifiques de niveau recherche, publiés ou non, émanant des établissements d'enseignement et de recherche français ou étrangers, des laboratoires publics ou privés.

# Modeling of Young's modulus variations with temperature of Ni and oxidized Ni using a magneto-mechanical approach.

Olivier HUBERT<sup>a,\*</sup>, Xavier MILHET<sup>b</sup>, Pascal GADAUD<sup>b</sup>, Mathieu TATAT<sup>b</sup>, Pierre-Olivier RENAULT<sup>b</sup>, Christophe COUPEAU<sup>b</sup>

<sup>a</sup>*LMT-Cachan (ENS-Cachan / CNRS UMR 8535 / Université Paris Saclay), 61 avenue du président Wilson, 94235 CACHAN Cedex, France*

<sup>b</sup>*Institut P', CNRS-ENSMA-Université de Poitiers, UPR 3346, B.P. 40109, FUTUROSCOPE CHASSENEUIL, Cedex 86961, Poitiers, France*

---

## Abstract

Thin films and coatings are usually used to give functional properties to the surface of the underlying substrate but are never seen as load bearing due to a very low film to substrate thickness ratio. However, this ratio can increase in some specific domains (such as transportation), where the weight reduction is a high stake. This study deals with the influence of the thermally grown oxide (TGO) NiO on the evolution of the elastic modulus of nickel with temperature. For pure nickel, the Young's modulus evolves non-linearly with temperature, from room temperature up to 360°C, corresponding to the Curie temperature of nickel. The amplitude of these variations can be drastically reduced with the presence of the NiO TGO. The purpose of this study is to propose a modeling of these phenomenon using magneto-mechanical approach. A first analytical modeling takes the change of the saturation magnetization, of the initial anhysteretic susceptibility and of the maximal magnetostriction with a relaxation of magneto-crystalline anisotropy concomitant to increasing temperature, into account. The second modeling is a numerical modeling giving the average behavior of a representative volume element. It allows a continuous description of the change with temperature of the Young's modulus and a clear interpretation of the effect of a coating. This gives an insight for future promising applications.

---

\*Corresponding author - hubert@lmt.ens-cachan.fr - ++33 1 47 40 22 24

*Keywords:* Nickel, Thermally-Grown-Oxide, *Delta E* effect, Magneto-mechanical coupling, Magnetostriction, Multiscale modeling, Residual stresses

---

## 1. Introduction

Thin films and coatings are generally used to give functional properties to the surface of the underlying substrate. For example, they play an important role of diffusion barriers to prevent the degradation of the substrate by oxidation when used at high temperature [1]; they can be used to prevent wear and erosion, or to provide lubrication and thermal insulation [2]. Various chemical and/or physical deposition techniques (with various compositions) can be used or they can develop naturally, resulting for example from the oxidation of the surface in a controlled atmosphere (thermally grown oxide TGO) [3]. Generally, these films are very thin and are not seen as load bearing. In some particular applications, such as turbine blades for example, the coating to substrate thickness ratio increases, inducing some peculiar mechanical behaviors as observed for Young's modulus variation of oxidized nickel in a recent study [4, 5]. The elastic modulus has been measured from 20°C up to 600°C. Its evolution with temperature is non-linear and non monotonous from room temperature up to 360°C, corresponding to the Curie temperature of nickel. But the amplitude of these variations can be drastically reduced by the TGO.

The non-monotonous Young's modulus evolution with temperature was previously reported by many authors [6, 7, 8], known as temperature dependent  $\Delta E$  effect. Its relation with the mechanical or magnetic state of material was discussed in the early work of Bozorth [6] who reported experiments from Siegel, Quimby and Köster [9].

The influence of TGO on this behavior was not reported since the work of Tatat [5] (except experiments of Huntz interpreted as internal stress rearrangement [10]) and no model was proposed to simulate the variation of pure nickel Young's modulus with temperature and model the influence of the oxide layer on this behavior. Actually, it was suspected to arise from a long-range modification of the internal stresses within the substrate. This interpretation seems accurate considering that stress is well known to change significantly the magnetic behavior [6, 7, 11] and the apparent Young's mod-

33 ulus of a wide range of magnetic materials [12].

34

35 The purpose of this paper is to propose a modeling of the variation of  
36 Young's modulus of Ni and Ni-NiO layers with temperature using a magneto-  
37 mechanical approach. As these approaches usually consider the influence of  
38 multiaxial stress on the magneto-mechanical behavior, they allow an accu-  
39 rate modeling of both Young's modulus (seen a stress *vs* strain ratio for a  
40 low stress amplitude) and internal stress effect. Experimental results are first  
41 reminded. Two modeling approaches are then proposed: an analytical mod-  
42 eling first based on a room temperature  $\Delta E$  effect modeling [12]; a numerical  
43 implementation is secondly detailed based on the work of Daniel [13] allowing  
44 a continuous description of the Young's modulus variations with temperature  
45 and taking the TGO, or any other coating nature leading to residual stresses,  
46 into account.

## 47 2. Experimental results and interpretation

### 48 2.1. Material and experimental features

49 A pure (>99%) 2 mm thick polycrystalline nickel has been used for the  
50 experimental study [4, 5]; the initial grain size of the Ni samples is about  
51 30  $\mu\text{m}$ . After a soft mechanical polishing, samples have been oxidized in  
52 synthetic air (80% nitrogen, 20% oxygen) during 1h30 at 1110°C to form  
53 NiO coatings and then furnace cooled at approximately 300°C/h. The spec-  
54 imen was exposed to an  $Ar - H_2$  flow to limit the oxidation prior to the  
55 target temperature and during cooling. The oxidation was simultaneously  
56 performed on the two opposite free surfaces of the Ni samples. After oxida-  
57 tion, the thickness of the NiO coatings has been estimated at 16  $\mu\text{m}$  thick  
58 (figure 1). Electron Back Scattered Diffraction (EBSD) measurements were  
59 carried out on a polished sample after oxidation (for a 40mm<sup>2</sup> area - 10mm  
60  $\times$  4mm). Figure 2 shows a typical example of inverse pole figure (with re-  
61 spect to the normal direction ND) obtained after oxidizing. The grain size of  
62 the Ni substrate has evolved substantially by growing up to about 280  $\mu\text{m}$ .  
63 Texture index concludes on the other hand to a quasi-isotropic distribution  
64 of orientations: the material can be considered as isotropic.

65 The elastic properties of the specimens were investigated from room tem-  
66 perature (RT) up to 600°C by means of the resonant frequency technique in  
67 bending mode [14] in the 1-10 kHz range (the temperature range 20°C to  
68 600°C was chosen in order to make sure to measure the material behavior

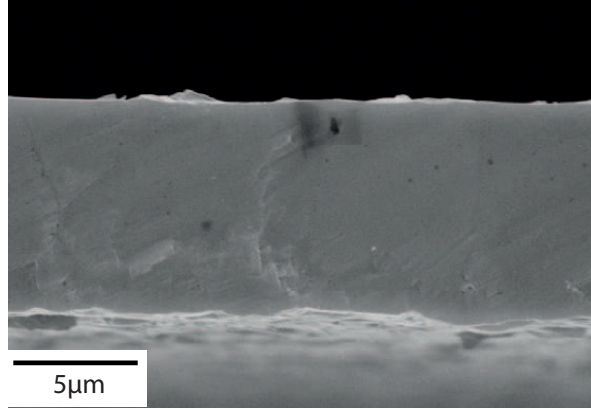


Figure 1: SEM observation of typical NiO oxide layer after oxidizing in synthetic air during 1h30 at 1110°C.

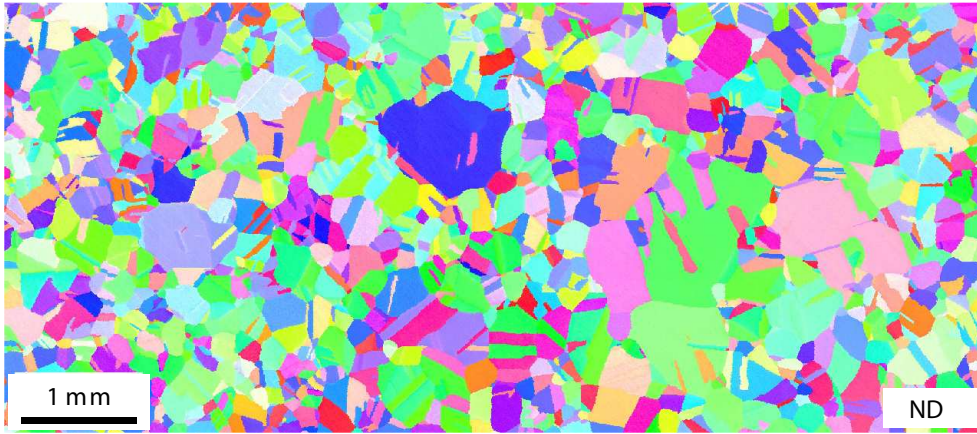


Figure 2: Inverse pole figure (normal direction ND) obtained by EBSD on the Ni sample after oxidizing treatment.

69 well above the Curie temperature). This method is detailed hereafter: In  
 70 the case of a bulk material, the longitudinal Young's modulus ( $E$ ) can be  
 71 deduced using the following relation [15]:

$$E = 0.9464\rho f^2 \frac{L^4}{h^2} \zeta \quad (1)$$

72 where  $f$  is the flexural resonance frequency,  $\rho$  the density,  $h$  and  $L$ , the

73 beam thickness (0.5 to 2 mm) and span length (20 to 30 mm), and  $\zeta$ , a  
74 correcting factor close to 1. The sample is maintained horizontally between  
75 steel wires located at the vibration nodes. Both excitation and detection  
76 are performed using an electrostatic device (capacitance created between the  
77 sample and a unique electrode). Using this set-up, the Young's modulus can  
78 be measured from  $-150^{\circ}\text{C}$  up to  $1100^{\circ}\text{C}$  without any harmful contact. The  
79 heating rate can be as low as  $1^{\circ}\text{C}/\text{min}$  and high vacuum ( $\approx 10^{-4}$  Pa) is used  
80 to hinder or limit the specimen oxidation. The accuracy of this method is  
81 better than 0.5% for conductive bulk materials whatever the rigidity range.  
82 An important feature of this technique lies in the very low applied stress  
83 level, less than 1 MPa.

84

## 85 2.2. Variation of Young's modulus

86 Figure 3 shows the evolution of the Young's modulus of the specimens  
87 with temperature [4]. The measurements reported here were performed us-  
88 ing the same Ni substrate; the Young's modulus was first measured on the  
89 laminated state before oxidation, secondly on the two-sides oxidized speci-  
90 men (*i.e.* two NiO coatings) and, finally, after removing one and both NiO  
91 coatings successively by fine polishing (noted as "peeled off samples" in the  
92 following). The procedure to remove the oxide, based on conventional met-  
93 allographic techniques, included an ultimate step of fine chemo-mechanical  
94 polishing in order to reach a very low roughness without work hardening *i.e.*  
95 no additional residual stresses in the sub-surface.

96 Two domains are clearly evidenced in figure 3, depending on the tempera-  
97 ture. Above approximately  $T = 360^{\circ}\text{C}$ , the evolution of the elastic modulus is  
98 quite similar regardless to the specimen state, characterized by the expected  
99 linear decrease of the Young's modulus with the temperature. A slight dif-  
100 ference between non-oxidized and oxidized substrates can be observed due  
101 to composite effect: the Young's modulus of NiO is usually higher than the  
102 Young's modulus of pure Ni; its value depends strongly on oxidizing temper-  
103 ature and oxide porosity [4]. It must be emphasized that the increase of the  
104 grain size from 30 to  $280\ \mu\text{m}$  does not act on the modulus of the substrate  
105 (the experimental technique integrates all the sample volume).

106

107 Below this threshold temperature, the Young's modulus depends strik-  
108 ingly on the structural configuration of the specimens:

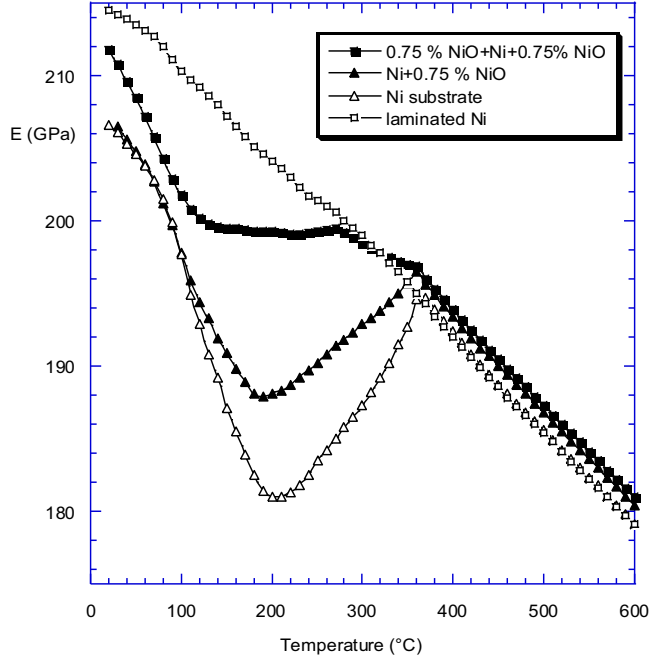


Figure 3: Variation of Young's modulus with temperature for different specimens.

- 109     • the presence of the NiO oxide layer representing only about 3% of the  
110     total thickness on the Ni substrate significantly influences the value of  
111     the elastic modulus (apparent Young's modulus  $E_a$ ) at a temperature  
112     range between 90°C and 360°C.
- 113     • the variation of the Young's modulus at 260°C for oxidized samples can  
114     be associated to the Néel temperature transition of NiO.
- 115     • the maximum deviation of  $E_a$  is about 9% between nickel-  
116     oxide.

### 117 2.3. Estimation of residual stresses

118     The residual stresses have been determined at RT using the X-ray diffrac-  
119     tion (XRD) so-called  $\sin^2\psi$  method [16] where  $\psi$  is defined as the angle be-  
120     tween the normal to the sample surface and the normal to the diffracting

121 planes. X-ray measurements were carried out using a four-circle diffractome-  
 122 ter (Seifert XRD 3003) operating at 40 kV and 40 mA, with a Cu X-ray tube  
 123 ( $\lambda_{K\alpha} = 0.15418$  nm) equipped with a  $1 \times 1$  mm<sup>2</sup> point focus and a Ni filter on  
 124 the direct beam path to absorb the Cu  $K\alpha$  radiation. The incident beam was  
 125 collimated using a collimator 1 mm in diameter and targeted on the samples  
 126 mounted on an Eulerian cradle for  $\psi$  tilting. The X-ray measurements have  
 127 been performed for fourteen different  $\psi$  angles for two independent plane  
 128 families, namely {331} and {420}. The residual stress state was calculated  
 129 from the lattice strains assuming a planar equibiaxial stress state and using  
 130 the X-ray elastic constants [17]. For a polycrystalline quasi-isotropic mate-  
 131 rial of Young's modulus  $E$  and Poisson's ratio  $\nu$ , the biaxial residual stress  
 132 state of magnitude  $\sigma^r$  is given by the slope of  $\sin(\theta)^{-1} = f(\sin^2\psi)$  function  
 133 following:

$$\frac{\sin(\theta_0)}{\sin(\theta)} = \sigma^r \left( \frac{(1 + \nu)\sin^2\psi - 2\nu}{E} \right) + 1 \quad (2)$$

134 where  $\theta$  and  $\theta_0$  indicate the Bragg's angle of the diffracting plane with  
 135 or without stress respectively. The technique was used to evaluate the resid-  
 136 ual stress level inside both the as-received material and the material after  
 137 oxidation [5]. In the as-received state the material exhibits a high level of  
 138 residual stress in sub-surface that corresponds to a biaxial compression of  
 139 amplitude  $-130 \pm 30$  MPa. This surface stress state should be equilibrated by  
 140 an internal bi-tension stress that can unfortunately not be estimated because  
 141 the transition area between these two fields cannot clearly be defined. It can  
 142 be considered that thermal treatment completely reduces this stress field to  
 143 zero since a global recrystallization mechanism occurs.

144  
 145 After oxidation, the internal stresses have only been determined in the  
 146 NiO coatings. Actually the X-Ray diffraction analysis is not possible in the  
 147 Ni layer due to the large grain size. Internal stresses in NiO correspond  
 148 to an equibicompaction of amplitude  $-550 \pm 50$  MPa [5]. Similar compressive  
 149 stresses values are reported in literature [10, 19]. They mainly result from the  
 150 thermal mismatch coefficients between the coating and the substrate. Indeed  
 151 dilatation coefficients for NiO and Ni are respectively:  $\alpha_{NiO} = 14.5 \times 10^{-6} \text{K}^{-1}$   
 152 and  $\alpha_{Ni} = 17.5 \times 10^{-6} \text{K}^{-1}$  [18, 19]. The thermal stresses distribution in the  
 153 Ni layer has been determined from a simple beam analysis integrating the  
 154 experimental values obtained for the oxide coatings thickness and residual  
 155 stress, and considering a global equilibrium (force and momentum equilib-

156 rium). For NiO-Ni-NiO system, the in-plane stress in the Ni substrate is a  
 157 bi-tension and remains constant over the entire thickness ( $+9\pm 1$  MPa), while  
 158 for Ni-NiO the stress decreases linearly from a bi-tension ( $+18\pm 2$  MPa) to  
 159 a bi-compression state ( $-9\pm 1$  MPa) giving an average value of  $+3\pm 1$  MPa.  
 160 After removal of the double oxide coating, it may be assumed that the Ni  
 161 layer is completely internal stress free.

162

163 As seen in figure 3 and table 1, internal stresses of few MPa are sufficient  
 164 to significantly modify the apparent Young's modulus of nickel. Results  
 165 reported in table 1 correspond to the estimated average biaxial stress inside  
 166 the Ni Layer.

Table 1: Change of  $\Delta E$  effect with biaxial residual stress level of amplitude  $\sigma^r$ .

Configuration	Cold rolled	2-sides oxidized	1-side oxidized	Peeled-off
$\Delta E/E(\%)$	0	-3	-8	-11
$\sigma^r$ (MPa)	unknown	+9	+3 (average)	0

#### 167 2.4. Results interpretation

168 The non monotonous change of Young's modulus with temperature and  
 169 effect of TGO cannot be explained by a classical mechanical rule of mixture  
 170 but by magneto-elastic considerations. Ni is a ferromagnetic material ex-  
 171 hibiting magnetic domains below its Curie temperature,  $T_C$ , equal to  $360^\circ\text{C}$   
 172 [6].

173 The observed evolution of pure Ni Young's modulus for increasing tem-  
 174 perature was already experimentally reported in literature [6, 7, 8]. This  
 175 deviation from the Hooke's law is known as the  $\Delta E$  effect (" $\Delta$ " for vari-  
 176 ation) and can only be highlighted in the very first stage of stress-strain  
 177 curves [13]. A relation with the magnetic character of the material can be  
 178 made considering:

- 179 1. The phenomenon is strongly dependent on the magnetization  $M$  of the  
 180 layer: at the magnetic saturation ( $M = M_s$ ;  $M_s$ : saturation magne-  
 181 tization of the material) the non-linear variation of Young's modulus  
 182 progressively vanishes.

183 2. Young's modulus recovers its linear variation with temperature above  
 184 the Curie temperature of the layer (360°C).

185 These points are illustrated in figure 4a.

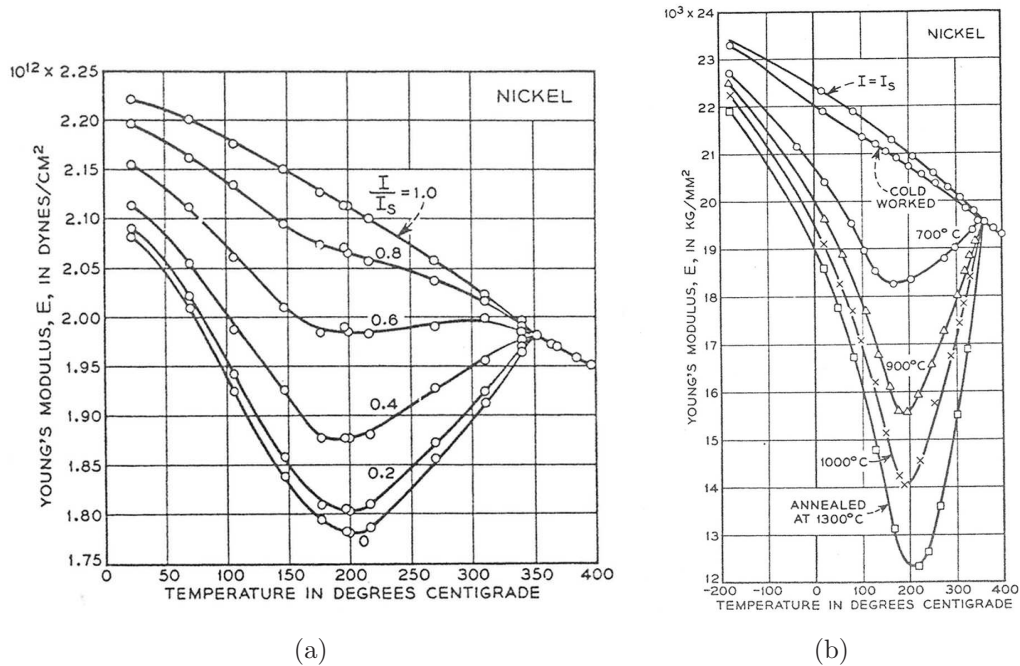


Figure 4: Apparent Young's modulus of nickel vs. Temperature: (a) effect of magnetization to saturation magnetization ratio ( $I/I_s$ ); (b) effect of mechanical condition ("internal stress") and thermal annealing [6] - NB:  $10^{12}[\text{Dynes/cm}^2]=10^2[\text{GPa}]$ ;  $10^3[\text{Kg/mm}^2]=9.81[\text{GPa}]\approx 10[\text{GPa}]$ .

186 As magnetic properties of ferromagnetic materials depend on the tem-  
 187 perature, the amplitude of  $\Delta E$  effect can change. In particular, the magne-  
 188 tocrystalline anisotropy (determining for a single crystal the most favorable  
 189 magnetization direction) decreases significantly while the temperature in-  
 190 creases, especially from RT up to 100°C for Ni [6]. Hence, with increasing  
 191 temperature, the magnetic moments direction becomes progressively more  
 192 sensitive to the mechanical stress, enhancing the  $\Delta E$  effect. From approxi-  
 193 mately  $T=200^\circ\text{C}$  to the Curie temperature, the spontaneous magnetization  
 194 (and consequently the magnetostriction) of Ni quickly decreases down to 0:  
 195 the ferromagnetic properties disappear (magnetostrictive and exchange con-  
 196 stants progressively decrease to zero). This latter point explains that the  $\Delta E$

197 effect is gradually weakened and vanishes at  $T_C$  when the material becomes  
198 paramagnetic.

199

200 The role of stress is another point to consider. For cold worked nickel (as  
201 received material), the decrease of Young's modulus is regular following a  
202 classical linear variation with temperature (figure 3). Thermal annealing at  
203 increasing temperature progressively enhances the non-linear phenomenon as  
204 experimentally observed and reported in figure 4b [6]. The internal stress as-  
205 sociated to plasticity acts as a magnetic saturation; the stress relieving at in-  
206 creasing annealing temperature acts as a demagnetization. The effect of oxide  
207 layers is another typical example of coupling to stress. X-rays measurements  
208 indicates that the substrate is submitted to residual stresses. Single-layer or  
209 two-layers situations do not lead to the same stress level. The amplitude of  
210 non-linearity of Young's modulus is changed. The highest amplitude of  $\Delta E$   
211 effect is reached for peeled off sample where residual stress reduces to zero.

212

213 Considering finally that the measurement method is based on a stress  
214 loading, a quantitative modeling of these phenomena requires to use a fully  
215 coupled magneto-mechanical approach and to consider the effect of temper-  
216 ature on the parameters involved in this coupling.

### 217 **3. Modeling**

#### 218 *3.1. $\Delta E$ effect definition*

219 The so-called  $\Delta E$  effect is one of the manifestations of magneto-elastic  
220 couplings in ferromagnetic materials [7]. It can be defined as the depen-  
221 dence of Young's modulus  $E$  of a material on its state of magnetization. The  
222 Young's modulus of an originally demagnetized specimen appears to be lower  
223 (by an amount  $\Delta E$ ) than the Young's modulus of the same specimen magne-  
224 tized at saturation (figure 5). Indeed a ferromagnetic material is subdivided  
225 in magnetic domains. A magnetic domain corresponds to microscopic or-  
226 ganization of magnetic moments aligned together to minimize the so-called  
227 exchange energy. Each magnetic domain is magnetized at saturation and  
228 characterized by a free isochoric strain called magnetostriction. Due to mag-  
229 neto crystalline energy, orientation of magnetic domains is usually associated  
230 to crystallographic axes (8 easy directions for nickel - 8 domain families). At  
231 zero applied stress or magnetic field and without boundary effect, domains  
232 are equally distributed so that the initial deformation and magnetization are

233 null. An increasing magnetic field leads to a progressive increase of the well  
 234 oriented domain families volume so that macroscopic magnetization and de-  
 235 formation occur (macroscopic magnetostriction  $\epsilon^\mu$ ). An increasing uniaxial  
 236 stress  $\sigma$  leads to a progressive increase of the well oriented domain fami-  
 237 lies of opposite sign so that a macroscopic magnetostriction  $\epsilon^\mu$  occurs while  
 238 macroscopic magnetization remains null.

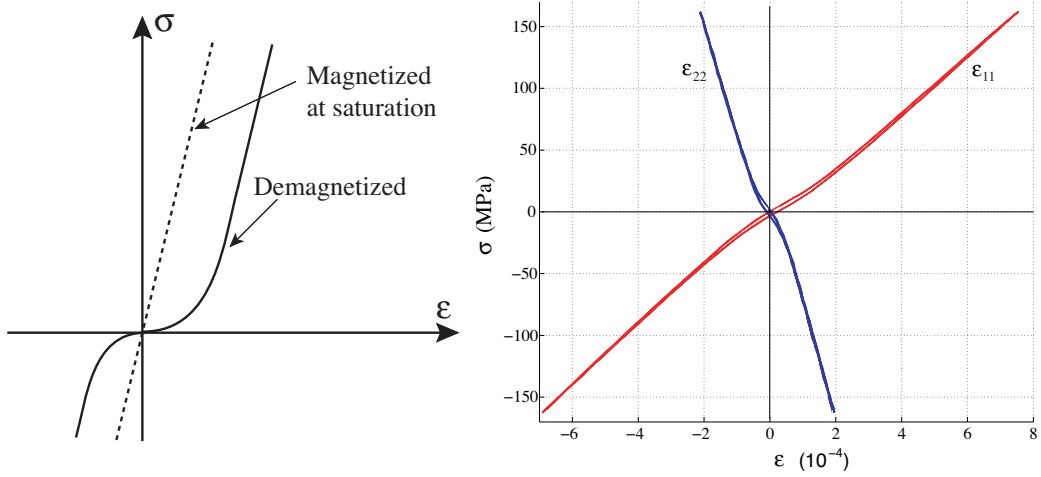


Figure 5: Illustration of the  $\Delta E$  effect for a tensile-compressive test ( $\epsilon$  is the total strain); (a) principle (b) illustration for iron-cobalt alloy [20].

This magnetostriction strain  $\epsilon^\mu$  is superimposed to the elastic strain  $\epsilon^{el}$ , so that the total measured strain  $\epsilon$  is higher than foreseen without magnetostriction phenomenon. It is defined by equation (3), all the strains being measured in the direction parallel to the applied stress.

$$\epsilon = \epsilon^\mu + \epsilon^{el} \quad (3)$$

Because  $\epsilon^\mu$  is usually non-linear with stress and saturates, the apparent Young's modulus appears non-linear and saturates too. The stress level investigated using the resonant technique for measurement of Young's modulus is very small ( $<1\text{MPa}$ ). The apparent Young's modulus  $E_a$  is given by:

$$E_a = \left( \left. \frac{d\epsilon^\mu}{d\sigma} \right|_{\sigma=0} + \left. \frac{d\epsilon^{el}}{d\sigma} \right|_{\sigma=0} \right)^{-1} \quad (4)$$

In case of a saturated material, the magnetic domain structure has reached a saturated configuration and the magnetostriction strain cannot evolve anymore. The apparent Young's modulus is then defined as:

$$E_a = \left. \frac{d\sigma}{d\epsilon^{el}} \right|_{\sigma=0} \quad (5)$$

239 leading to a higher value because  $\frac{d\epsilon^\mu}{d\sigma}$  is always positive [12]. This phe-  
 240 nomenon is described by Bozorth [6] and reported in figure 4. In case of a  
 241 highly deformed material, the internal stresses saturate the magnetostriction  
 242 leading to the same effect.

### 243 3.2. Analytical modeling of apparent Young's modulus

244 An analytical modeling of the  $\Delta E$  effect at RT has been recently proposed  
 245 [12]. This approach is inspired from a multiscale model for the prediction of  
 246 magneto-elastic reversible behavior of ferromagnetic materials presented in  
 247 [13] and in Appendix A. The full multiscale model is used for a numerical  
 248 resolution in section 4. The simplified approach is limited to the situation  
 249 where no magnetic field is applied, so that the magneto-static energy does  
 250 not appear in the definition of the magnetic equilibrium. On the other hand  
 251 it has been supposed that the magneto-crystalline anisotropy energy does  
 252 not participate to the evolution of the magnetostriction strain. In such con-  
 253 ditions, the elastic energy is the only energy term explicitly considered in the  
 254 description of the magnetic equilibrium of a domain.

255  
 256 On the other hand, an isotropic polycrystal can be seen as an aggregate  
 257 of single crystals with random orientation. Polycrystal can be considered  
 258 as a single crystal for which all directions would be easy directions. In one  
 259 domain of such a single crystal, the magnetostriction strain tensor can be  
 260 written (in its own framework):

$$\epsilon_m^\mu = \frac{1}{2} \lambda_{max} \begin{pmatrix} 2 & 0 & 0 \\ 0 & -1 & 0 \\ 0 & 0 & -1 \end{pmatrix} \quad (6)$$

261  $\lambda_{max}$  denotes the maximum magnetostriction strain of the considered  
 262 polycrystal.

263 A multiaxial eigen-stress tensor is considered in the macroscopic frame  
 264  $(\vec{e}_1, \vec{e}_2, \vec{e}_3)$  following:

$$\boldsymbol{\sigma} = \begin{pmatrix} \sigma_{11} & 0 & 0 \\ 0 & \sigma_{22} & 0 \\ 0 & 0 & \sigma_{33} \end{pmatrix} \quad (7)$$

265 The transformation matrix from macroscale to domain scale is given by:

$$\mathbf{P} = \begin{pmatrix} \cos\theta \sin\varphi & \sin\theta & \cos\theta \cos\varphi \\ \sin\theta \sin\varphi & -\cos\theta & \sin\theta \sin\varphi \\ \cos\varphi & 0 & -\sin\varphi \end{pmatrix} \quad (8)$$

266 leading to:

$$\boldsymbol{\epsilon}_p^\mu = {}^t \mathbf{P} \boldsymbol{\epsilon}_m^\mu \mathbf{P} \quad (9)$$

267 The magneto-elastic energy is given for a constant by:

$$W_\sigma^\alpha = -\boldsymbol{\sigma} : \boldsymbol{\epsilon}_p^\mu \quad (10)$$

that can be expressed as function of strain and stress components following:

$$W_\sigma^\alpha = -\frac{\lambda_{max}}{2} (\sigma_{11}(3 \cos^2\theta \sin^2\varphi - 1) + \sigma_{22}(3 \sin^2\theta \sin^2\varphi - 1) + \sigma_{33}(3 \cos^2\varphi - 1)) \quad (11)$$

268 Angles  $\theta$  ( $0-2\pi$ ) and  $\varphi$  ( $0-\pi$ ) define the orientation of domain in the macro-  
269 scopic frame.

270

271 Considering homogeneous stiffness, localization operation is avoided. The  
272 average magnetostriction is given by:

$$\boldsymbol{\epsilon}^\mu = \int_\alpha f_\alpha \boldsymbol{\epsilon}_p^\mu \quad (12)$$

273  $f_\alpha$  indicates the volume fraction of domain  $\alpha$  (see equation A.8 in Ap-  
274 pendix A) calculated using:

$$f_\alpha = \frac{\exp(-A_s \cdot W_\sigma^\alpha)}{\int_0^{2\pi} \int_0^\pi \exp(-A_s \cdot W_\sigma^\alpha) \sin\varphi \, d\varphi \, d\theta} \quad (13)$$

with (see equation A.11 in Appendix A):

$$A_s = \frac{3\chi_0(T)}{\mu_0 M_s(T)^2} \frac{T^{RT}}{T} \quad (14)$$

275  $\chi_0$  and  $M_s$  are the initial anhysteretic susceptibility (variation of anhys-  
 276 teretic magnetization with magnetic field) and saturation magnetization.  $\mu_0$   
 277 is the vacuum permeability ( $=4\pi \times 10^{-7}$  Henry/m).  $T$  indicates the actual  
 278 temperature and  $T^{RT}$  the room temperature.

279 A tensile test of magnitude  $\sigma$  along the macroscopic unit vector  $\vec{e}_3$  is now  
 280 considered. The magneto-elastic energy expression is simplified into:

$$W_\sigma^\alpha = -\frac{1}{2}\lambda_{max}\sigma (3 \cos^2\varphi - 1) \quad (15)$$

281 The magnetostriction strain tensor is diagonal:

$$\epsilon^\mu = \frac{\pi \lambda_{max} S_2}{2 S_1} \exp\left(-\frac{1}{2}A_s\lambda_{max}\sigma\right) \begin{pmatrix} -1 & 0 & 0 \\ 0 & -1 & 0 \\ 0 & 0 & 2 \end{pmatrix} \quad (16)$$

with

$$S_1 = 2\pi \exp\left(-\frac{1}{2}A_s\lambda_{max}\sigma\right) \int_0^\pi \exp\left(\frac{3}{2}A_s\lambda_{max}\sigma\cos^2\varphi\right) \sin\varphi d\varphi \quad (17)$$

282 and,

$$S_2 = \int_0^\pi (3 \cos^2\varphi - 1) \exp\left(\frac{3}{2}A_s\lambda_{max}\sigma\cos^2\varphi\right) \sin\varphi d\varphi \quad (18)$$

283 The apparent Young's modulus is measured by the resonance method cor-  
 284 responding to a low magnitude tensile loading. Considering the additivity of  
 285 deformation (homogeneous stress) at a physical point, the apparent Young's  
 286 modulus verifies:

$$\frac{1}{E_a} = \frac{1}{E} + \frac{1}{E_m} \quad (19)$$

287 with  $E$  the ideal Young's modulus and  $E_m$  the magnetostriction modulus.  
 288 The latter satisfies:

$$\frac{1}{E_m} = \left. \frac{d\epsilon_{33}^\mu}{d\sigma} \right|_{\sigma=0} \quad (20)$$

289 Since an analytical expression of magnetostriction *vs* stress is available,  
 290 the calculation is developed:

$$\epsilon_{33}^{\mu} = \frac{\pi \lambda_{max} S_2(\sigma)}{S_1(\sigma)} \exp\left(-\frac{1}{2} A_s \lambda_{max} \sigma\right) \quad (21)$$

A derivation of  $\epsilon_{33}^{\mu}$  function with respect to stress at  $\sigma = 0$ , leads to, after few calculations:

$$\frac{1}{E_m} = \left. \frac{d\epsilon_{33}^{\mu}}{d\sigma} \right|_{\sigma=0} = \frac{\lambda_{max}^2 A_s}{5} = \frac{3\chi_0(T)\lambda_{max}^2 T^{RT}}{5\mu_0 M_s(T)^2 T} \quad (22)$$

291 Most of the terms are temperature dependent, including  $\lambda_{max}$ , that may  
 292 lead to a complex variation of the magnetostriction modulus with temper-  
 293 ature. It is possible to extend the proposed approach to other hypotheses  
 294 than homogeneous stiffness by reporting the localization operation in the  
 295 definition of  $\lambda_{max}$ . This point is addressed in the next section.

### 296 3.3. Numerical applications for pure isotropic polycrystalline nickel and in- 297 fluence of temperature

298 The parameter  $\lambda_{max}$  can be derived from magnetostrictive constants of  
 299 single crystal  $\lambda_{100}$  and  $\lambda_{111}$  following different assumptions, depending of ei-  
 300 ther or not the magnetization rotation is considered, and depending on the  
 301 elastic behavior of the domain (single crystal stiffness constants) and the  
 302 average medium. An analytical calculation of the average magnetostrictive  
 303 tensor can be strictly made only at magnetic saturation, when the magne-  
 304 tization is uniformly aligned along the external field direction. Grains  $g$  are  
 305 composed of single domains  $\alpha$  so that the magnetostriction strain in each  
 306 grain is the magnetostriction strain of the domain in the crystallographic  
 307 frame (CF) :

$$\epsilon_{\mu}^g = \epsilon_{\mu}^{\alpha} = \frac{3}{2} \begin{pmatrix} \lambda_{100}(\gamma_1^2 - \frac{1}{3}) & \lambda_{111}\gamma_1\gamma_2 & \lambda_{111}\gamma_1\gamma_3 \\ \lambda_{111}\gamma_1\gamma_2 & \lambda_{100}(\gamma_2^2 - \frac{1}{3}) & \lambda_{111}\gamma_2\gamma_3 \\ \lambda_{111}\gamma_1\gamma_3 & \lambda_{111}\gamma_2\gamma_3 & \lambda_{100}(\gamma_3^2 - \frac{1}{3}) \end{pmatrix}_{CF} \quad (23)$$

The average magnetostriction strain is the solution of a thermo-elasticity problem [21]:

$$\epsilon_{\mu}^{sat} = \langle {}^t\mathbb{B}^g : \epsilon_{\mu}^g \rangle \quad (24)$$

308 where  ${}^t\mathbb{B}^g$  indicates the transpose of the stress concentration tensor and  
 309  $\langle .. \rangle$  denotes the averaging operation over the volume. The macroscopic  
 310 behavior being isotropic, previously defined equation (6) gives the average  
 311 saturation magnetostriction strain tensor with  $\lambda_{max} = \lambda_{sat}$  the saturation  
 312 magnetostriction. In case of high magneto crystalline anisotropy, domain  
 313 wall displacement and magnetization rotation can be considered as succes-  
 314 sive (they are usually considered as concomitant) so that it is possible to  
 315 estimate another average magnetostriction tensor denoted average *maximal*  
 316 magnetostriction strain tensor. A calculation of analytical values is possible  
 317 using  $\lambda_{100} = 0$  for  $\langle 111 \rangle$  easy directions materials or  $\lambda_{111} = 0$  for  $\langle 100 \rangle$   
 318 easy directions materials:

- in case of low magneto crystalline energy (free rotation) or at the mag-  
netic saturation:

$$\lambda_{max} = \lambda_{sat} = \frac{2}{5}\lambda_{100}k^a + \frac{3}{5}\lambda_{111}k^b$$

319 This value corresponds to the theoretical magnetostriction at the mag-  
 320 netic saturation.

- in case of high magneto crystalline energy (no rotation):

$$\begin{aligned} \lambda_{max} &= \frac{2}{5}\lambda_{100}k^a && \text{for materials with} \\ &&& \langle 100 \rangle \text{ easy directions} \\ \lambda_{max} &= \frac{3}{5}\lambda_{111}k^b && \text{for materials with} \\ &&& \langle 111 \rangle \text{ easy directions} \end{aligned}$$

321  $k^a$  and  $k^b$  are homogenization parameters depending on the elastic prop-  
 322 erties. They are given by:

$$\begin{cases} k^a &= \frac{\mu_a}{\mu_{eff}} \frac{\mu_{eff} + \mu^*}{\mu_a + \mu^*} \\ k^b &= \frac{\mu_b}{\mu_{eff}} \frac{\mu_{eff} + \mu^*}{\mu_b + \mu^*} \end{cases} \quad (25)$$

323  $\mu_a$  and  $\mu_b$  are the the single crystal shear moduli (equation 26 - with  
 324  $C_{ij}$  the stiffness constants of the cubic symmetry single crystal).  $\mu_{eff}$  is the  
 325 shear modulus of the effective medium given by equation (27).  $\mu^*$  (eq. 28)  
 326 is the Hill's shear modulus, whose definition depends on  $\mu_o$  and  $\kappa_o$  the shear

327 and compression moduli of the reference medium supposed isotropic (NB:  
 328  $\kappa_o = \kappa$ ).

$$\begin{cases} \mu_a &= \frac{1}{2}(C_{11} - C_{12}) \\ \mu_b &= \frac{1}{2}C_{44} \\ \kappa &= \frac{1}{3}(C_{11} + 2C_{12}) \end{cases} \quad (26)$$

$$\mu_{eff} = \frac{5(\mu_a + \mu^*)(\mu_b + \mu^*)}{(3\mu_a + 2\mu_b + 5\mu^*)} - \mu^* \quad (27)$$

$$\mu^* = \frac{1}{6}\mu_o \frac{9\kappa_o + 8\mu_o}{\kappa_o + 2\mu_o} \quad (28)$$

329 The value of these parameters (and finally of  $k^a$  and  $k^b$ ) depends on the  
 330 homogenization approximations made:

- 331 • Homogeneous stress (Reuss hypothesis - *ie*:  $\mu_o=0$ ):  $k^a = k^b = 1$
- 332 • Homogeneous deformation (Voigt hypothesis - *ie*:  $\mu_o = \infty$ ):  $k^a =$   
 333  $5\mu_a/(2\mu_a + 3\mu_b)$  and  $k^b = 5\mu_b/(2\mu_a + 3\mu_b)$
- 334 • Hashin and Shtrikman upper estimation (*ie*:  $\mu_o = \mu_b$  - considering that  
 335  $\mu_b > \mu_a$ )
- 336 • Hashin and Shtrikman lower estimation (*ie*:  $\mu_o = \mu_a$  - considering that  
 337  $\mu_b > \mu_a$ )
- Self-consistent estimation (*ie*:  $\mu_o = \mu_{eff}$  so that  $\mu_{eff}$  is the result of  
 the self-consistent equation:

$$8\mu_{eff}^3 + (9\kappa + 4\mu_a)\mu_{eff}^2 - (12\mu_a\mu_b + 3\kappa\mu_b)\mu_{eff} - 6\kappa\mu_a\mu_b = 0 \quad (29)$$

338 Analytical expressions of  $k_a$  and  $k_b$  are not reported for the three last  
 339 estimations due to their complicated expressions.

340 *3.3.1. Apparent Young's modulus at the room temperature*

341 The physical constants for nickel used for the calculations are reported in  
 342 table 2. They are given at RT. The value of the second magneto crystalline  
 343 constant  $K_2$  strongly varies from one author to another (from one value  
 344 to its opposite) [6, 7]. The effect of this term is usually negligible when its  
 345 amplitude is close or inferior to the amplitude of the first magneto crystalline  
 346 constant  $K_1$ . Equation (30) gives the magneto crystalline energy expression  
 347 function of constants  $K_1$  and  $K_2$  and direction cosines  $\gamma_i$  of magnetization in  
 348 the crystal frame.

$$W_K^\alpha = K_1(\gamma_1^2\gamma_2^2 + \gamma_2^2\gamma_3^2 + \gamma_3^2\gamma_1^2) + K_2(\gamma_1^2\gamma_2^2\gamma_3^2) \quad (30)$$

349 The magneto elastic energy can be calculated for a uniaxial stress  $\sigma_u$   
 350 along the direction [100] of the single crystal and a magnetostriction strain  
 351 at the domain scale (23). It gives:

$$W_\sigma^\alpha = -\frac{1}{2}\lambda_{100}\sigma_u (3 \gamma_1^2 - 1) \quad (31)$$

352 To estimate if rotation has to be or not taken into account at RT, a  
 353 material with positive  $K_1$  ( $< 100 >$  easy magnetization direction) and a  
 354 magnetization rotation of angle  $\theta$  in the  $(\vec{e}_1, \vec{e}_2)$  plane are considered. The  
 355 magnetoelastic and magnetocrystalline energy of a domain  $\alpha_1$  oriented along  
 356  $\vec{e}_1$  can be written following:

$$\begin{cases} W_K^{\alpha_1} &= K_1(\cos\theta^2 \sin\theta^2) \\ W_\sigma^{\alpha_1} &= -\frac{1}{2}\lambda_{100}\sigma_u(3\cos\theta^2 - 1) \end{cases} \quad (32)$$

357 If no other magnetization mechanism or energy is considered, the varia-  
 358 tion of total energy is null at equilibrium so that:

$$\frac{dW_K^{\alpha_1}}{d\theta} = -\frac{dW_\sigma^{\alpha_1}}{d\theta} \quad (33)$$

359 An equalization of the two expressions for  $\theta = 0$  allows to estimate an  
 360 uniaxial stress amplitude  $\sigma_u$  able to initiate a magnetization rotation. Its  
 361 expression is reported in equation (34).

$$\sigma_u \approx \left| \frac{2K_1}{3\lambda_{100}} \right| \quad (34)$$

362 Using the numerical values reported in table 2, a stress  $\sigma_u$  higher than 100  
 363 MPa is obtained. This value is much larger than the value expected during

364 the Young's modulus measurements (less than 1 MPa). The no rotation  
 365 assumption can be made at RT so that  $\lambda_{max}$  is defined by:

$$\lambda_{max} = \frac{3}{5}\lambda_{111}k_b \quad (35)$$

Table 2: Physical constants of pure nickel at RT [6, 7]; see figure 10 for  $\chi_0$  value.

$K_1$	$K_2$	$M_s$	$\lambda_{100}$	$\lambda_{111}$	$\chi_0$	$C_{11}$	$C_{12}$	$C_{44}$
$-5 \times 10^3$	$\pm 2 \times 10^3$	$4.84 \times 10^5$	-50	-25	800	246	147	248
J.m <sup>-3</sup>	J.m <sup>-3</sup>	A/m	ppm	ppm	-	GPa	GPa	GPa

366 Assuming finally an effective Young's modulus  $E$  of 223 GPa (in accor-  
 367 dance with  $C_{ij}$  values), different estimations of the apparent Young's modulus  
 368 can be made depending on the different estimations of  $k_b$ . They are reported  
 369 in the following table:

Table 3: Different estimations of  $k_b$ ,  $\lambda_{max}$ ,  $E_m$ ,  $E_a$  and  $\Delta E/E(\%) = (E_a - E)/E \times 100$  at RT - magnetostriction is given in ppm ( $\times 10^{-6}$ ) and moduli in GPa - V: Voigt estimation, R: Reuss estimation, HS+: Hashin-Shtrikman upper estimation, HS-: Hashin-Shtrikman lower estimation, SC: self-consistent estimation.

	V	HS+	SC	HS-	R
$k_b$	1.316	1.209	1.187	1.151	1
$\lambda_{max}$	-19.7	-18.1	-17.8	-17.3	-15.0
$E_m$	1573	1866	1934	2057	2726
$E_a$	195	199	200	201	206
$\Delta E/E(\%)$	-12.4	-10.7	-10.3	-9.8	-7.6

370 The sequence of estimations reported in the table is classical. Values  
 371 are roughly consistent with the experimental results reported in figure 3  
 372 and [5, 6]. The homogeneous stress hypothesis giving an apparent Young's  
 373 modulus of 206 GPa leads nevertheless to the best result. Since the EBSD  
 374 measurement did not reveal any crystallographic texture, this result could  
 375 be linked to an anisotropic distribution of domains.

376 3.3.2. Effect of increasing temperature on apparent Young's modulus

377 Temperature has a significant effect on the physical constants of nickel  
 378 used in the analytical modeling.

- 379 • Figure 6 shows the experimental results obtained by Kirkham [22] and  
 380 Döring reported in [6] for the magnetostriction of a polycrystalline  
 381 nickel (confirmed by the more recent measurements of Tatsumoto [23]).  
 382 Magnetostriction is decreasing with increasing temperature. It reaches  
 383 zero at  $T_C$ . No data are available for single crystal parameters  $\lambda_{100}$   
 384 and  $\lambda_{111}$ . One admissible assumption is to suppose that they behave  
 385 similarly than the saturation magnetostriction of the isotropic medium.  
 386  $\lambda_{max}$  would evolve similarly.

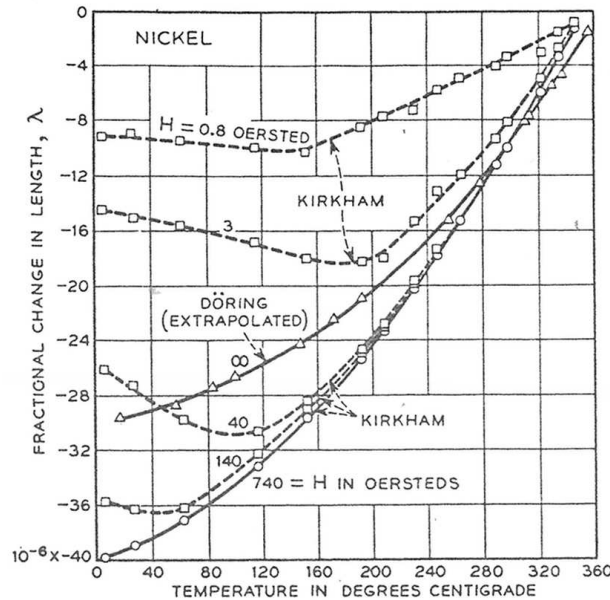


Figure 6: Effect of temperature on the magnetostriction of polycrystalline nickel [6, 22].

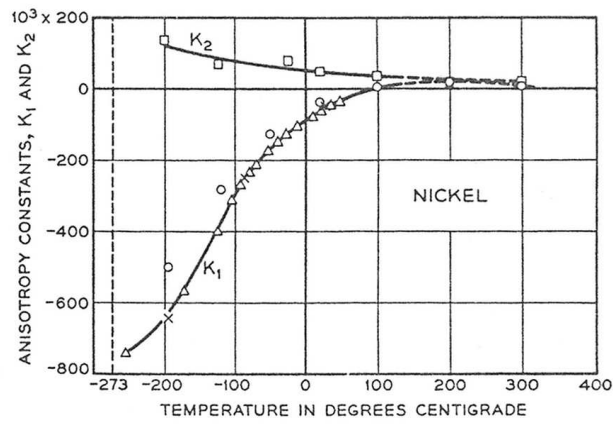
- 387 • Figure 7 shows the experimental results obtained by Honda [6] and  
 388 Tatsumoto [24] for the magnetostriction constants of nickel. The am-  
 389 plitude of constants decreases drastically with increasing temperature.  
 390  $K_1$ , initially negative, reaches zero at approximately 100°C for Honda

391 or 200°C for Tatsumoto, then becomes slightly positive before coming  
392 back to zero close to  $T_C$ .  $K_2$  is positive and of lower amplitude than  
393  $K_1$ . It decreases regularly to zero when temperature is approaching  
394  $T_C$ .

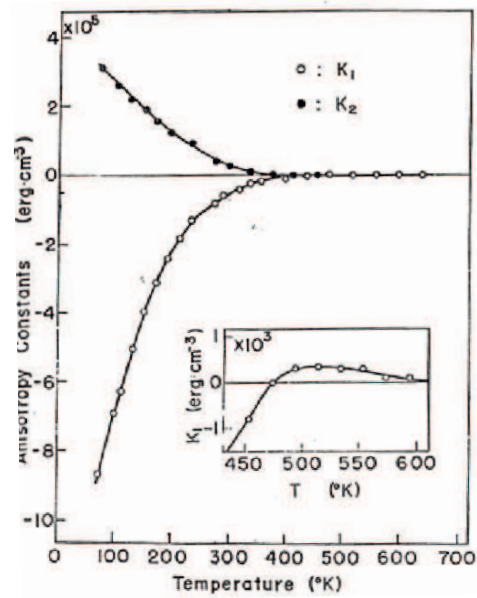
395 • Figure 8 shows the experimental results obtained by Kneller and re-  
396 ported by Ascher [25] for the saturation magnetization of nickel. The  
397 decrease of  $M_s$  with temperature is much less regular than magne-  
398 tostrictive and magneto crystalline constants.  $M_s$  remains high up to  
399 a high temperature level. It drastically decreases to zero when the  
400 temperature approaches  $T_C$ .

401 • Finally, figure 9 shows the experimental results obtained by Kirkham  
402 [22] for the initial susceptibility of nickel. A global strong increase  
403 of susceptibility before a sharp decrease at  $T_C$  is observed. The ini-  
404 tial increasing is strongly modified by a non monotonous evolution at  
405 a temperature (local maximum at  $T \approx 200^\circ\text{C}$ ) that is interpreted by  
406 Kirkham as a direct effect of the change of  $K_1$  sign (modifying the easy  
407 magnetization axis from the  $\langle 111 \rangle$  to the  $\langle 100 \rangle$  direction). The  
408 evolution of this term can be seen as a result of a new magnetic equilib-  
409 rium associated to new physical constants, as for Young's modulus. It  
410 must be noticed that the susceptibility used in the analytical modeling  
411 is the *anhysteretic* initial susceptibility, but the data reported are the  
412 initial susceptibility of the first magnetization curve. Figure 10 reports  
413 the typical cyclic and anhysteretic behaviors of pure polycrystalline  
414 nickel measured at RT. The initial susceptibility of the first magne-  
415 tization curve is drastically different from initial susceptibility of the  
416 anhysteretic curve. At RT, initial susceptibility of the first magnetiza-  
417 tion curve is close to 60 (in accordance with Kirkham measurements)  
418 while initial susceptibility of the anhysteretic curve is at minimum ten  
419 times higher (about 800). The variations with temperature of initial  
420 susceptibility of the first magnetization curve give only a survey of the  
421 anhysteretic susceptibility variations.

422 Let reconsider now the analytical expression of  $E_m$  equation 22, tempera-  
423 ture dependent parameters are:  $\lambda_{max}$ ,  $\chi_0$  and  $M_s$ .  $K_1$  quickly decreases while  
424 the temperature increases, meaning that the rotation becomes progressively  
425 dominant (for a temperature around 100°C up to 200°C). The maximum



(a)



(b)

Figure 7: Effect of temperature on the magnetocrystalline constants of nickel - (a) results of Honda [6]; (b) results of Tatsumoto [24] - NB:  $K_1$  and  $K_2$  are given in  $\text{erg}/\text{cm}^3 - 10 [\text{erg}/\text{cm}^3] = 1 [\text{J}/\text{m}^3]$ .

426 magnetostriction definition has to be reconsidered because it tends progres-

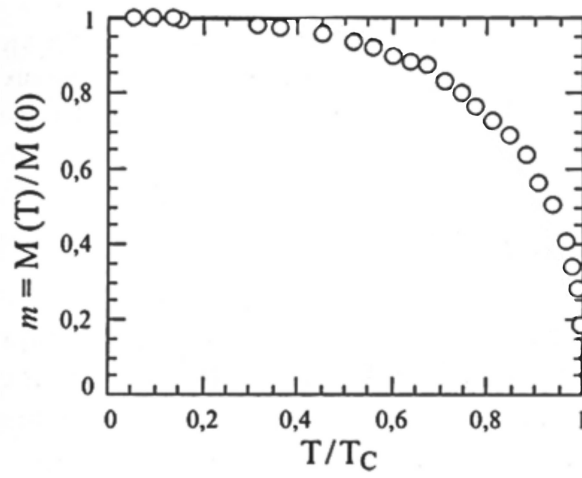


Figure 8: Effect of temperature on the saturation magnetization of nickel [25].

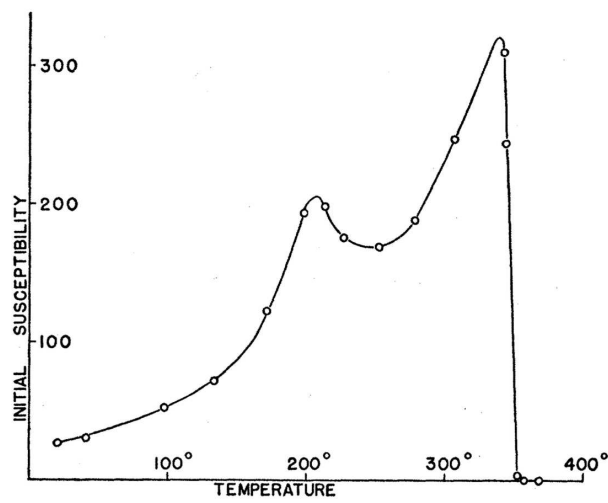


Figure 9: Effect of temperature on the initial susceptibility of nickel [22].

427 sively to the saturation magnetostriction:

$$\lambda_{max} = \frac{2}{5}\lambda_{100}k_a + \frac{3}{5}\lambda_{111}k_b \quad (36)$$

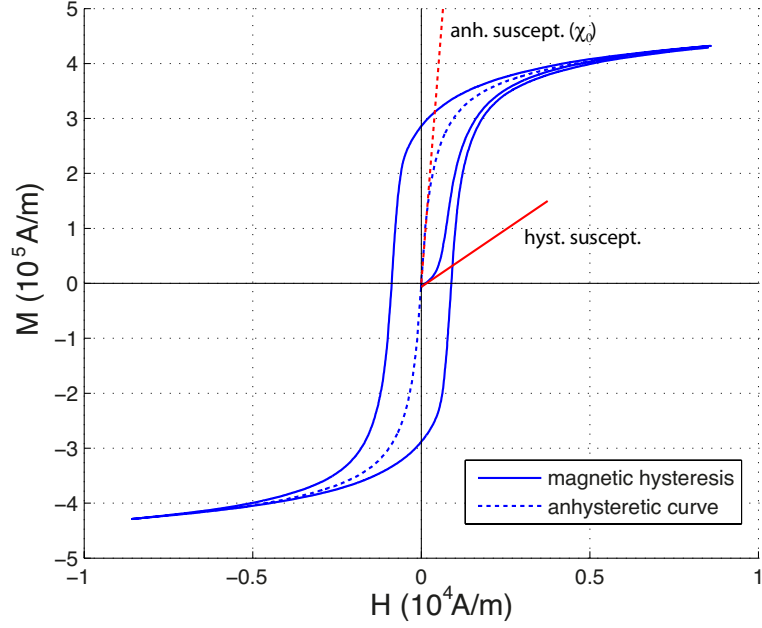


Figure 10: Typical cyclic and anhysteretic behaviors of pure polycrystalline nickel at RT.

428 Variations of  $\lambda_{100}$  and  $\lambda_{111}$  with temperature must be taken into account  
 429 too. They are considered to follow the same variation with temperature than  
 430  $\lambda_s$  plotted in figure 6.

431 Variation of the anhysteretic initial susceptibility  $\chi_0$  with temperature is un-  
 432 known since figure 9 refers to the hysteretic initial susceptibility. To simplify,  
 433 a linear increasement of  $\chi_0$  with temperature is considered:

$$\chi_0(T) = \chi_0^{RT} \frac{T}{T_{RT}} \quad (37)$$

434 Such relation is in global accordance with the experimental variation  
 435 of hysteretic initial susceptibility and allows a simplification of the mag-  
 436 netostriction modulus expression:

$$\frac{1}{E_m} = \frac{3\chi_0^{RT}}{5\mu_0} \left( \frac{\lambda_{max}(T)}{M_s(T)} \right)^2 \quad (38)$$

437 Therefore new assessments of the magnetostriction modulus can be ob-  
 438 tained considering the different previous estimations at a temperature of

439 200°C. Parameters values at this temperature come from experimental re-  
 440 sults. They are reported in table 4.

Table 4: Physical constants of pure nickel at 200°C used for the estimation of the apparent Young's modulus (a linear variation of the ideal Young's modulus with temperature has been used to estimate the  $C_{ij}$  values using equation (40) - Poisson's ratio variations are not considered);  $\chi_0$  is supposed unchanged with temperature.

$M_s$	$\lambda_{100}$	$\lambda_{111}$	$\chi_0$	$C_{11}$	$C_{12}$	$C_{44}$
$3.9 \times 10^5$	-33.3	-16.7	800	227	136	229
A/m	ppm	ppm	-	GPa	GPa	GPa

441 The effective Young's modulus  $E$  is 206 GPa at 200°C (in accordance with  
 442  $C_{ij}$  values and experimental results). Different estimations of the apparent  
 443 Young's modulus can be made depending on the different estimations of  $k_a$   
 444 and  $k_b$ . They are reported in table 5.

Table 5: Different estimations of  $k_a$ ,  $k_b$ ,  $\lambda_{max}$ ,  $E_m$ ,  $E_a$  and  $\Delta E/E(\%) = (E_a - E)/E \times 100$  at 200°C - magnetostriction is given in ppm ( $\times 10^{-6}$ ) and moduli in GPa - V: Voigt estimation, R: Reuss estimation, HS+: Hashin-Shtrikman upper estimation, HS-: Hashin-Shtrikman lower estimation, SC: self-consistent estimation.

	V	HS+	SC	HS-	R
$k_a$	0.525	0.687	0.719	0.773	1
$k_b$	1.316	1.209	1.187	1.151	1
$\lambda_{max}$	-20.2	-21.3	-21.5	-21.8	-23.3
$E_m$	977	881	863	835	731
$E_a$	170	167	166	165	161
$\Delta E/E(\%)$	-17.4	-19.0	-19.3	-19.8	-22.0

445 Whatever the estimation, a decrease of the apparent Young's mod-  
 446 ulus with temperature is clearly observed. This decrease fluctuates be-  
 447 tween 36 MPa and 45 MPa depending on the estimation. These values are  
 448 in good agreement with values observed in figure 3 and those reported in [6]  
 449 (figure 4a and 4a after annealing). It can be noticed that the homogeneous  
 450 stress estimation leads now to the lowest apparent Young's modulus (it was  
 451 corresponding to the highest value for the calculations at RT). Homogeneous

452 stress estimation allows to get the highest variation of  $\Delta E$  effect with temper-  
453 ature. On the other hand it is interesting to compare these values with those  
454 reported in table 6, where the no rotation condition has been maintained. A  
455 clear increase of the apparent Young's modulus is observed, that does not fit  
456 to the experimental results. It confirms that the variation of the apparent  
457 Young's modulus with temperature is due to a combined effect of variation  
458 of intrinsic physical constants and a relaxation of the magnetization rotation  
459 enhancing the magnetostriction strain variation with stress.

460  
461 The Young's modulus remains to its effective value (196 MPa) when tem-  
462 perature reaches the Curie temperature (disappearance of ferromagnetic cou-  
463 pling), leading to the sharp increase of apparent Young's modulus.

Table 6: Different estimations of  $k_b$ ,  $\lambda_{max}$ ,  $E_m$ ,  $E_a$  and  $\Delta E/E(\%) = (E_a - E)/E \times 100$  at 200°C **using the no-rotation condition**:  $\lambda_{max} = \frac{3}{5}\lambda_{111}k_b$  - magnetostriction is given in ppm ( $\times 10^{-6}$ ) and moduli in GPa - V: Voigt estimation, R: Reuss estimation, HS+: Hashin-Shtrikman upper estimation, HS-: Hashin-Shtrikman lower estimation, SC: self-consistent estimation.

	V	HS+	SC	HS-	R
$k_b$	1.316	1.209	1.187	1.151	1
$\lambda_{max}$	-13.2	-12.1	-11.9	-11.5	-10.0
$E_m$	2289	2715	2813	2993	3966
$E_a$	189	191	192	193	196
$\Delta E/E(\%)$	-8.3	-7.1	-6.8	-6.4	-4.9

#### 464 4. Numerical implementation of $E(T)$ and comparisons between 465 experiments and modeling

##### 466 4.1. Multiscale model and simulation of apparent Young's modulus at the 467 room temperature

468 The variations of nickel physical constants with temperature are now  
469 considered to propose a modeling of  $E_a(T)$  curve and compare it to the  
470 measurements. The previous calculations used the assumption of no effect of  
471 magnetization rotation on the magnetostrictive response. This assumption  
472 is acceptable for a high  $K_1$ . When  $K_1$  reaches 0, this assumption is not valid

473 anymore. The analytical modeling can be made on the other hand when  $\lambda_{max}$   
 474 is known. The definition of  $\lambda_{max}$  is nevertheless not unique (known only for  
 475 free rotation or no rotation situations). These different arguments motivate  
 476 the choice of a numerical approach.

477 A multiscale (MS) model originally dedicated to build magneto-mechanical  
 478 constitutive laws for anisotropic polycrystalline media is used [13]. The main  
 479 characteristics of this model are recalled in Appendix A. MS model involves  
 480 three scales: domain scale, grain scale and polycrystalline scale (representa-  
 481 tive volume element - *RVE*). Initially proposed by [26] at the grain scale,  
 482 it was extended to polycrystals by [13] and [27]. In the present study, an  
 483 isotropic grain distribution has been used (546 grains [13]). This model al-  
 484 lows, among others, to simulate the  $\Delta E$  effect of nickel ( $\epsilon_{33}^{\mu}(\sigma)$ ) as reported in  
 485 figure 11 where the effect of homogeneous stress or self consistent conditions  
 486 are compared.

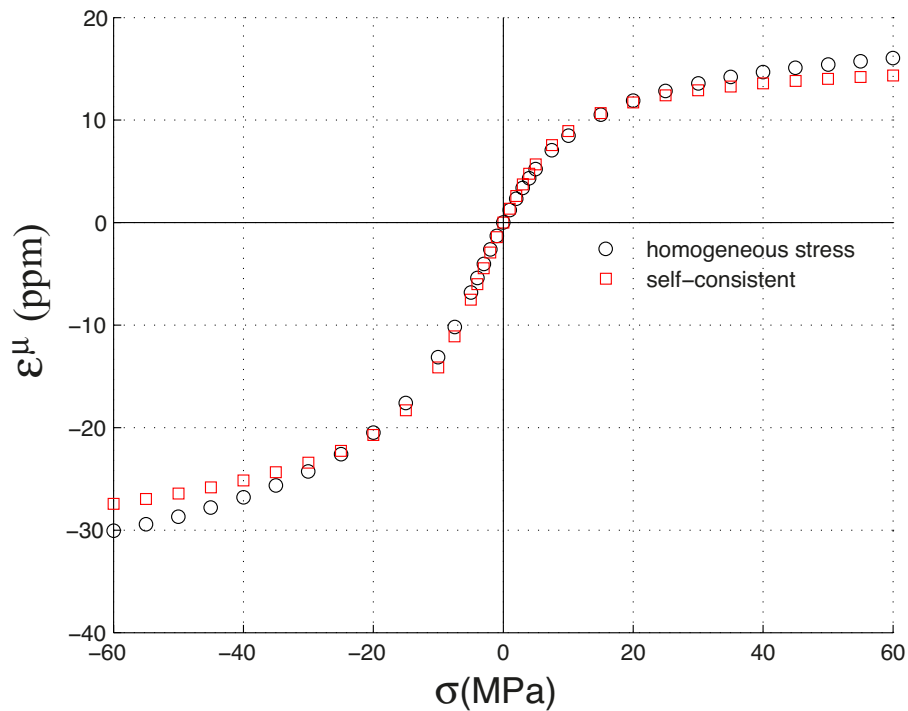


Figure 11:  $\Delta E$  effect for isotropic polycrystalline nickel as estimated by MS model at RT for homogeneous stress and self-consistent conditions.

487 The difference of slope a zero applied stress between the two simulations  
488 is low: a slope of  $1.212 \times 10^{-12} \text{Pa}^{-1}$  is obtained for the homogeneous stress  
489 condition and of  $1.345 \times 10^{-12} \text{Pa}^{-1}$  for the self-consistent condition. These  
490 values correspond to  $E_m^{-1}$ . The corresponding apparent Young's modulus is  
491 evaluated to 176 GPa and 172 GPa respectively (for a ideal Young's modu-  
492 lus of 223 GPa). These values are lower than the experimental values at RT  
493 reported in figure 3 and different from the value obtained after the analyti-  
494 cal approach (206 GPa for homogeneous stress estimation and 200 GPa for  
495 the self-consistent one) which considered that rotation was not occurring at  
496 RT. Another estimation by the analytical approach of the apparent Young's  
497 modulus at RT has been made, now considering a free rotation mechanism  
498 (*i.e.*  $\lambda_{max} = \frac{2}{5}\lambda_{100}k_a + \frac{3}{5}\lambda_{111}k_b$ ). The different estimations of  $E_a$  (numerical  
499 and analytic approaches for homogeneous stress and self-consistent estima-  
500 tions) are reported in table 7. The analytical estimation considering a free  
501 magnetization rotation leads to results closer to the numerical solution than  
502 the no-rotation assumption, especially for the self-consistent estimation. The  
503 variation of magnetostriction with stress must be considered as the result of  
504 both wall displacement and magnetization rotation at RT.

Table 7: Various estimations of apparent Young's moduli  $E_a$ (GPa) T=20°C. R: homoge-  
neous stress: SC: self-consistent

R num.	SC num.	R no rot.	SC no rot.	R rot.	SC rot.
176	172	206	200	154	162

#### 505 4.2. Simulation of $E_a(T)$ for isotropic polycrystalline nickel

506 The simulation of the apparent Young's modulus with temperature re-  
507 quires to use relations between physical constants (ideal Young's modu-  
508 lus, magnetostriction, magnetocrystalline constant, saturation magnetiza-  
509 tion) and temperature. Some of these relations have a theoretical back-  
510 ground, others have been built in former papers by different authors so that  
511 they fit properly the experimental data. The following functions are pro-  
512 posed:

- Ideal Young's modulus - All experiments (recent and former) show a linear decrease of ideal Young's modulus  $E$  with temperature  $T$ .

The following linear relation is implemented in the model:

$$E = E_0 - k_0T \quad (39)$$

513 with  $E_0=237.6$  GPa: Young's modulus at 0K;  $k_0=0.06603$  GPa/K.  
 514 Figure 12 allows the comparison between the linear approximation and  
 515 the experimental results. The same relation is used to consider the  
 516 variation of  $C_{ij}$  stiffness constants with temperature (in the range of  
 517 temperature considered in this paper):

$$C_{ij}(T) = C_{ij}(T^{RT}) \frac{E(T)}{E(T^{RT})} \quad (40)$$

- Saturation magnetization - the theoretical variation of the saturation magnetization  $M_s$  with temperature is given by the self-consistent equation [32]:

$$\frac{M_s}{M_{s0}} = \tanh\left(\frac{M_s/M_{s0}}{T/T_C}\right) \quad (41)$$

518 with  $M_{s0}$  the magnetization at 0K ( $M_{s0}=4.956 \times 10^5$  A/m). The tem-  
 519 perature  $T$  is expressed in Kelvin.

520 Figure 13 allows the comparison between the experimental and modeled  
 521 evolution of the saturation magnetization with the temperature. The  
 522 model gives high quality results.

- Magnetocrystalline constants - The variation of magnetocrystalline constant  $K$  with temperature has been studied theoretically by Zener [28]. It is expressed as function of magnetization ratio,  $K^0$  the magnetocrystalline constant at 0K, and a constant  $n$ :

$$K(T) = K^0 (M_s/M_s^0)^n \quad (42)$$

527  $n=10$  for a cubic symmetry. This value is justified considering that the  
 528 amplitude of magneto crystalline  $K_1$  is higher than the amplitude of  
 529  $K_2$ , and considering the cubic symmetry ( $4^{th}$  order of direction cosines).  
 530 This model is denoted model 1.

531 It has been shown that this relation did not fit very well the experi-  
 532 mental results obtained for nickel. The relation has been modified by

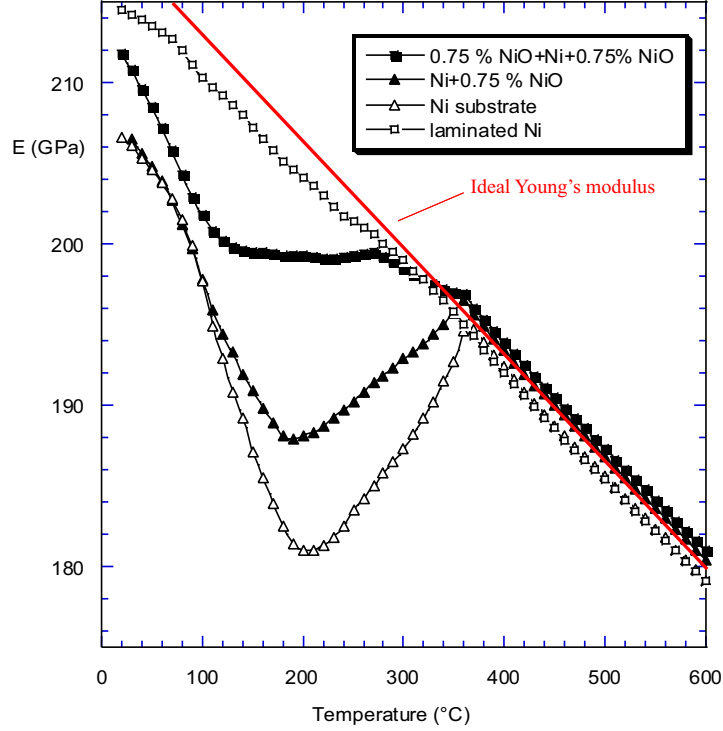


Figure 12: Variation of Young's modulus with temperature for different specimens complemented by a linear approximation of ideal Young's modulus.

533 Carr [30] to take account of the change of sign of  $K_1$  and an earlier  
 534 decrease of magneto crystalline amplitude. This model is denoted  
 535 model 2.

$$K(T) = K^0 \left( \frac{M_s}{M_s^0} \right)^n \left( 1 - \alpha \frac{T}{T_C} \right) \quad (43)$$

536 with  $n=10$  and  $\alpha > 1$

Williams and Bozorth [6] proposed on the other hand to use the following empirical relation to define the evolution of magneto crystalline constants with temperature:

$$K(T) = K^0 \exp(-kT^2) \quad (44)$$

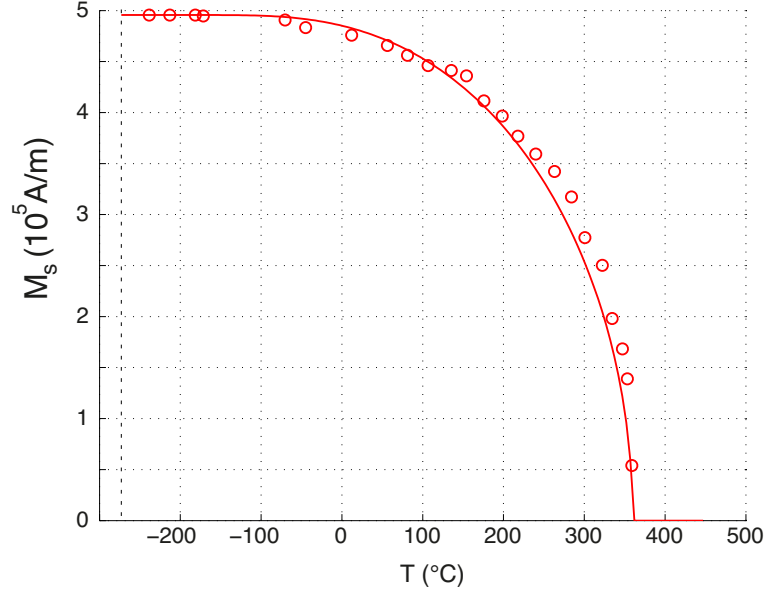


Figure 13: Comparison between experiment (circles) and modeling (full line - see eq. 41) of the evolution of saturation magnetization with temperature.

537 It has been decided to use this formulation multiplied by a linear func-  
538 tion of temperature in order to represent the change of sign of  $K_1$ . This  
539 model denoted model 3 is given by:

$$K_1(T) = K_1^0 \exp(-k_1 T^2) \left(1 - \alpha \frac{T}{T_C}\right) \quad (45)$$

540 with:  $K_1^0 = -82 \times 10^3 \text{ J/m}^3$ ,  $k_1 = 1.562 \times 10^{-5} \text{ K}^{-2}$ ,  $\alpha = 1.338$ .

541 Figure 14 gathers experimental points from various authors [6, 24, 29]  
542 and the results of the three models. The figure 15 is a zoom of figure  
543 14. Model 3 gives clearly the best results.

544

Following Williams and Bozorth [6], equation (46) has been used to  
model the variations of  $K_2$  with temperature:

$$K_2(T) = K_2^0 \exp(-k_2 T^2) \quad (46)$$

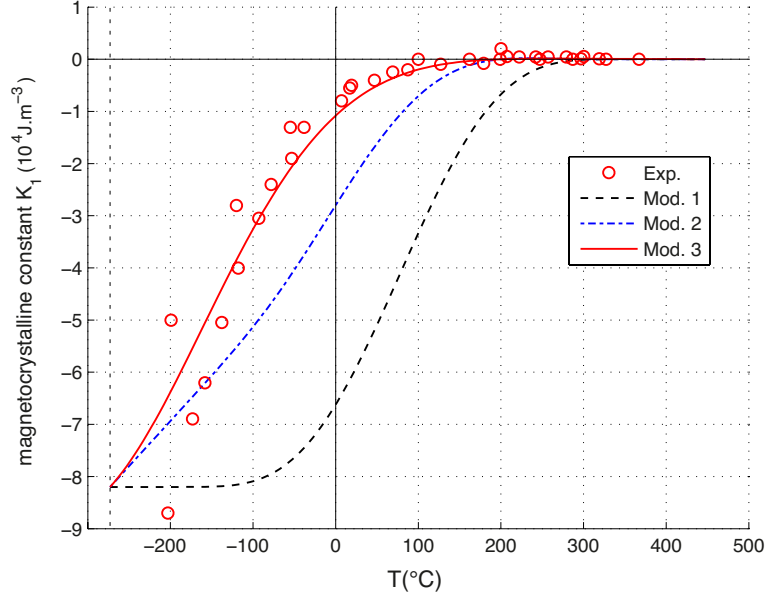


Figure 14: Comparison between experimental and modeled variation of  $K_1$  with temperature.

545 with:  $K_2^0 = \pm 28 \times 10^3 \text{ J/m}^3$ ,  $k_2 = 2.78 \times 10^{-5} \text{ K}^{-2}$ .

546

547  $K_2^0$  will be considered either positive or negative during the modeling  
 548 since the sign of  $K_2$  is controversial. Figure 16 gathers experimental  
 549 points from various authors [6, 24] (including a negative estimation  
 550 from [31]) and results of the model. The sensitivity of magnetostriction  
 551 modulus to the  $K_2$  sign has to be estimated to verify if this uncertainty  
 552 is significant or not.

- 553 • Magnetostriction constants - No theoretical relation between magne-  
 554 tostriction and temperature is available in literature. A polynomial  
 555 variation is chosen to model the saturation magnetization of isotropic  
 556 polycrystal:

$$\lambda_s(T) = \lambda_s^i (1 - (T/T_C)^m) \quad (47)$$

557 with  $\lambda_s^i = -32 \times 10^{-6}$  and  $m = 3.4$ . Extension of this function to  $\lambda_{100}$  and  
 558  $\lambda_{111}$  constants is considered, leading to:

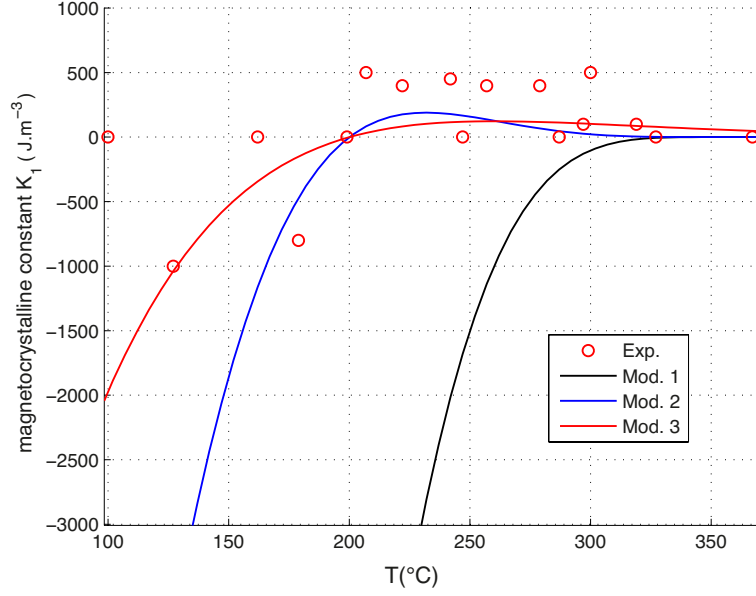


Figure 15: Comparison between experimental and modeled variation of  $K_1$  with temperature - zoom of figure 14.

$$\lambda_{100}(T) = \lambda_{100}^i (1 - (T/T_C)^m) \quad (48)$$

$$\lambda_{111}(T) = \lambda_{111}^i (1 - (T/T_C)^m) \quad (49)$$

559 with  $\lambda_{100}^i = -54 \times 10^{-6}$  and  $\lambda_{111}^i = -27 \times 10^{-6}$  so that the values at RT cor-  
 560 respond to classical values ( $-50 \times 10^{-6}$  and  $-25 \times 10^{-6}$  respectively). Re-  
 561 sults are plotted in figure 17 showing a good ability of the function to  
 562 model the experimental data.

563 These various functions are introduced in the multiscale model (Ap-  
 564 pendix A). In order to estimate the magnetostriction modulus, the multi-  
 565 scale model is employed to model the effect of a small stress magnitude (*i.e.*  
 566  $\Delta\sigma_{33} = 0.1 \text{ MPa}$ ) on the magnitude of macroscopic magnetostriction  $\Delta\epsilon_{33}^\mu$ . It  
 567 leads to:

$$\frac{1}{E_m} = \left. \frac{d\epsilon_{33}^\mu}{d\sigma} \right|_{\sigma=0} \approx \left. \frac{\Delta\epsilon_{33}^\mu}{\Delta\sigma_{33}} \right|_{\sigma_{33}=0} \quad (50)$$

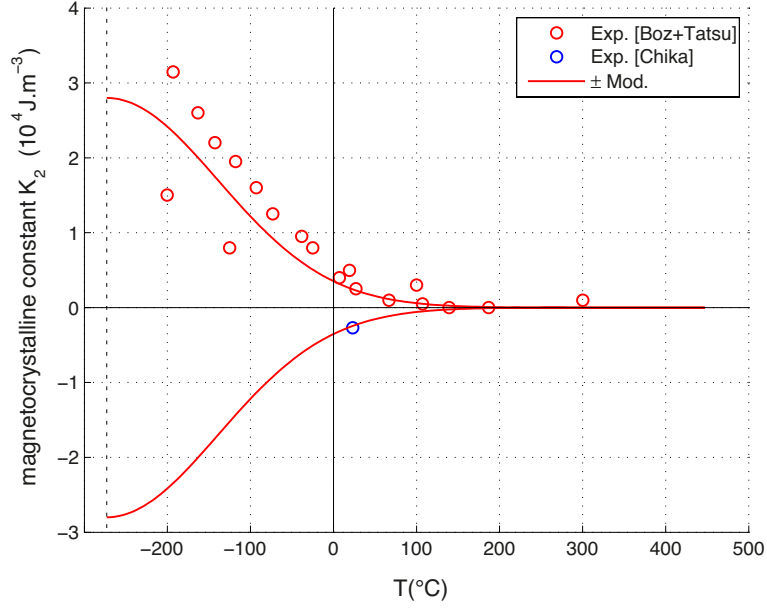


Figure 16: Comparison between experimental and modeled variation of  $K_2$  with temperature.

The apparent Young's modulus  $E_a$  satisfies the rule of mixture:

$$\frac{1}{E_a} = \frac{1}{E} + \frac{1}{E_m} \quad (51)$$

568 The variation of apparent Young's modulus for isotropic polycrystalline  
569 nickel with temperature is finally plotted in figure 18 using a homogeneous  
570 stress assumption and in figure 19 for the self-consistent condition. Plotted  
571 curves correspond to multiscale model (MS), analytical model without rota-  
572 tion, and analytical model with free rotation. The results obtained using the  
573 MS model are qualitatively in good agreement with the experimental results  
574 with a first decrease with temperature followed by a strong increase  
575 up to the Curie temperature. The temperature corresponding to the min-  
576 imum apparent Young's modulus is in accordance with experimental data.  
577 The global level of apparent Young's modulus is lower than expected from  
578 the room temperature up to 200°C, and the self-consistent approach leads  
579 to a clear underestimation of the Young's modulus variation. It can be ob-  
580 served by the way that the analytical model leads to a large (too large) frame

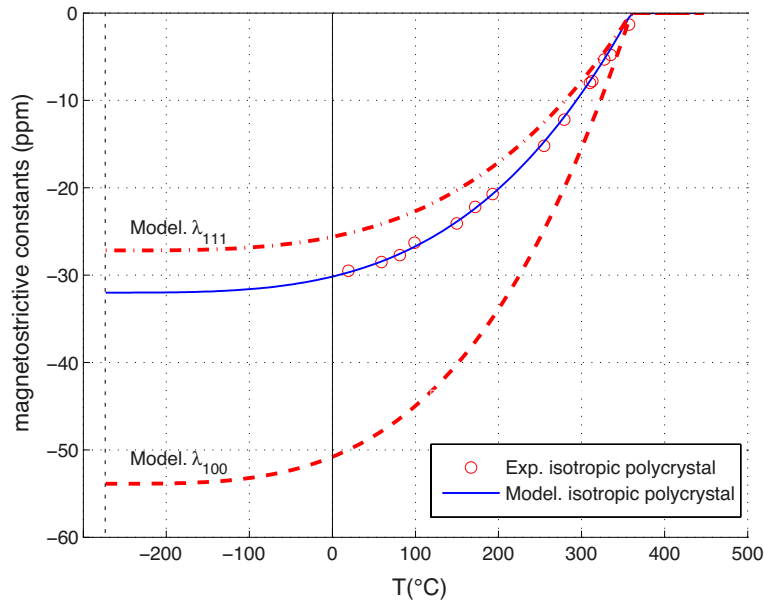


Figure 17: Comparison between experiment (circles) and modeling (full line) of the saturation magnetostriction with temperature. Representation of  $\lambda_{100}(T)$  and  $\lambda_{111}(T)$  functions.

581 of the MS solution in both cases for temperatures below 200°C. Above this  
 582 temperature, analytical results do not frame the solution anymore (especially  
 583 for the homogeneous stress estimation) indicating that the wall displacement  
 584 mechanism hypothesis used to get the analytical modeling is not applicable  
 585 any more. Since the homogeneous stress assumption gives results closer to  
 586 experiments, it has been used for the next simulations.

587 Because of uncertainties concerning the  $K_2$  anisotropy constant, it has been  
 588 decided to simulate the situation where  $K_2(T)$  is the exact opposite of pre-  
 589 vious function and the situation where  $K_2(T) = 0$ . Behaviors are plotted  
 590 in figure 20 (using homogeneous stress condition). A very small change is  
 591 observed meaning that  $K_2$  is a second order parameter. It has been kept  
 592 positive for the next simulations.

593 Reasons that explain the discrepancy between experiment and model-  
 594 ing are numerous: representativity of RVE, various uncertainties on physical  
 595 values,.... The main drawback is associated to the high uncertainty on the  
 596 variation of initial anhysteretic susceptibility with temperature and a possi-  
 597 ble anisotropic initial distribution of domains. It must finally be kept in mind

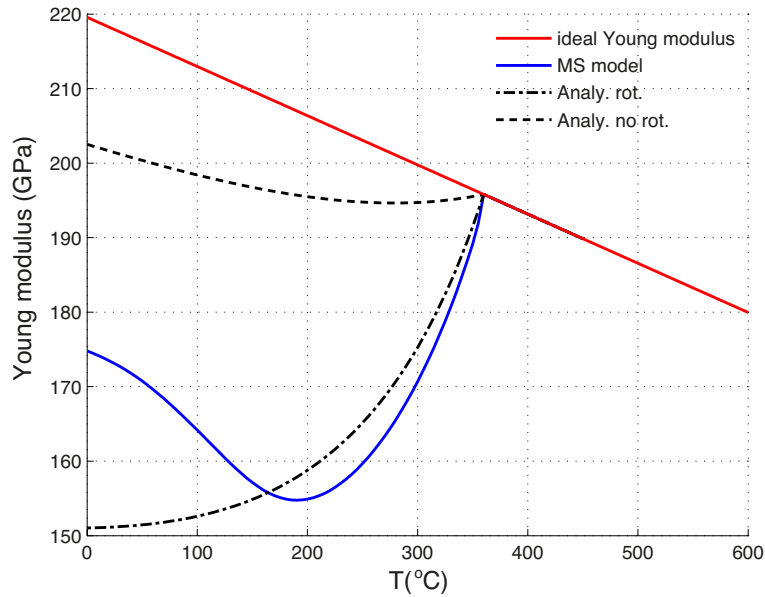


Figure 18: Change of nickel Young's modulus with temperature - ideal and apparent Young's modulus - homogeneous stress estimation.

608 that the mechanical loading used to measure the apparent Young's modu-  
 609 lus cannot be considered as an *anhysteretic* loading, meaning that compar-  
 600 isons between modeling and experiments should be considered at this step  
 601 as mainly qualitative comparisons, waiting for a hysteretic version of the  
 602 modeling (see [33, 34] for propositions of extension to hysteretic modeling).

#### 603 4.3. Simulation of NiO coating effects

604 The experimental measurements reported in figure 3 show that the "stiff-  
 605 ening" effect magnitude below  $T_C$  highly varies depending on the sample  
 606 state (as-received, two sides oxidized, single side oxidized, peeled-off oxide)  
 607 to another. To highlight and explain that effect, the following points have to  
 608 be considered:

- 609 • nickel has a larger dilatation coefficient than the oxide.
- 610 • oxide is formed at high temperature ( $T_{Ox}=1100^\circ\text{C}$ ).
- 611 • for any temperature below  $T_{Ox}$ , the oxide layer is in compression on  
 612 the nickel.

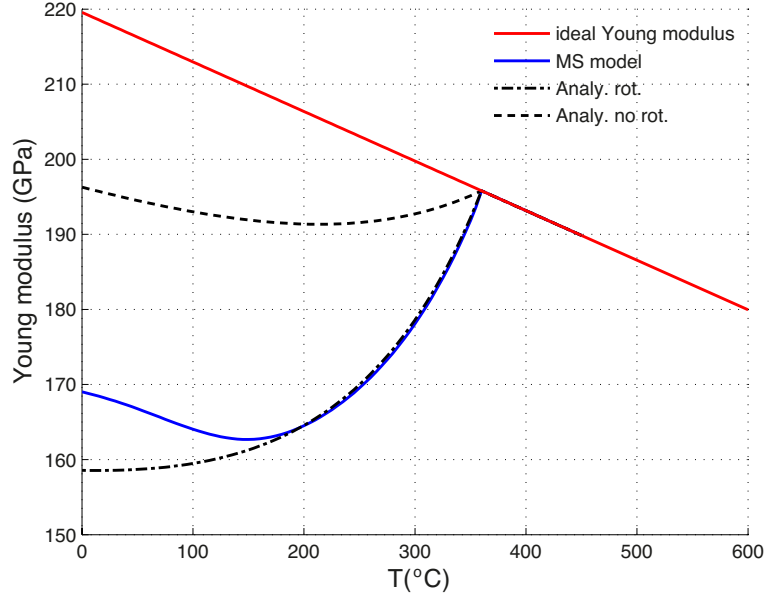


Figure 19: Change of nickel Young's modulus with temperature - ideal and apparent Young's modulus - self-consistent estimation.

- the mechanical balance states that the nickel layer is submitted to an equibitension residual stress of amplitude  $\sigma_0$ .

$$\boldsymbol{\sigma}_r = \begin{pmatrix} 0 & & \\ & \sigma_0 & \\ & & \sigma_0 \end{pmatrix}$$

613 Experimental XRD measurements reported in section 2.3 and provided  
614 at RT enable the estimation of  $\sigma_0$  magnitude for the 1-side oxidized and the  
615 2-sides oxidized situations. For NiO-Ni-NiO system,  $\sigma_0$  is homogeneous in  
616 the nickel layer and has been estimated to +9 MPa. For Ni-NiO, stress is  
617 heterogeneous across the thickness. Overall the average value in the nickel  
618 layer has been estimated to +3 MPa. For a more accurate modeling, it must  
619 be taken into account that  $\sigma_0$  depends on temperature since it decreases  
620 theoretically to zero at  $T_{Ox}$ . The following parametric formula can be used:

$$\sigma_0(T) = \sigma_0^0 - qT \quad (52)$$

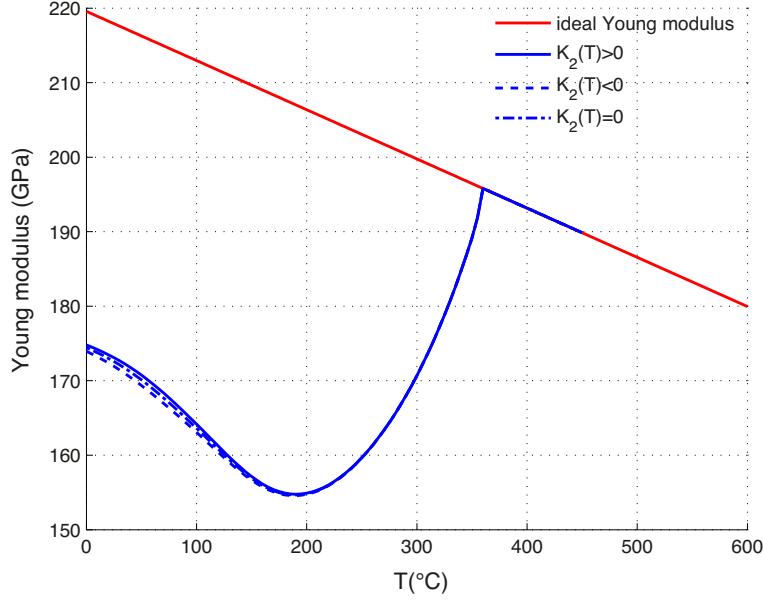


Figure 20: Change of nickel Young's modulus with temperature - effect of  $K_2$  magneto crystalline constant - homogeneous stress estimation.

621 with  $\sigma_0^0 = \{11.42, 3.81\}$  MPa and  $q = \{8.25, 2.75\} \times 10^{-3}$  MPa/K for the {2-sides  
 622 oxidized , 1-side oxidized} situations respectively.  $\sigma_0(T)$  functions are plot-  
 623 ted in figure 21 in the temperature range of experiments.

624

625 The residual stress tensor is introduced in the multiscale model as a con-  
 626 stant external loading (the relaxation of this stress with the magnetostriction  
 627 strain of the sample is not considered). The procedure explained above is  
 628 used to extract the magnetostriction modulus variations with temperature.  
 629 Results are plotted in figure 22. The expected saturation effect is observed.  
 630 The amplitude reduction is lower than observed experimentally. Uncertain-  
 631 ties on the residual stress level and other approximations are probably at the  
 632 origin of these discrepancies.

633 In order to estimate the sensitivity to higher stress, the model has been  
 634 tested for a superimposed constant uniaxial applied stress  $\sigma_{33} = \sigma_a$ . Results  
 635 are illustrated in figure 23 where  $\sigma_a$  varies from 5MPa to 50MPa exhibiting  
 636 the mechanical saturation phenomenon already discussed in literature [6] and  
 637 reported in figures 3 (as received material) and 4b (cold rolled sample).

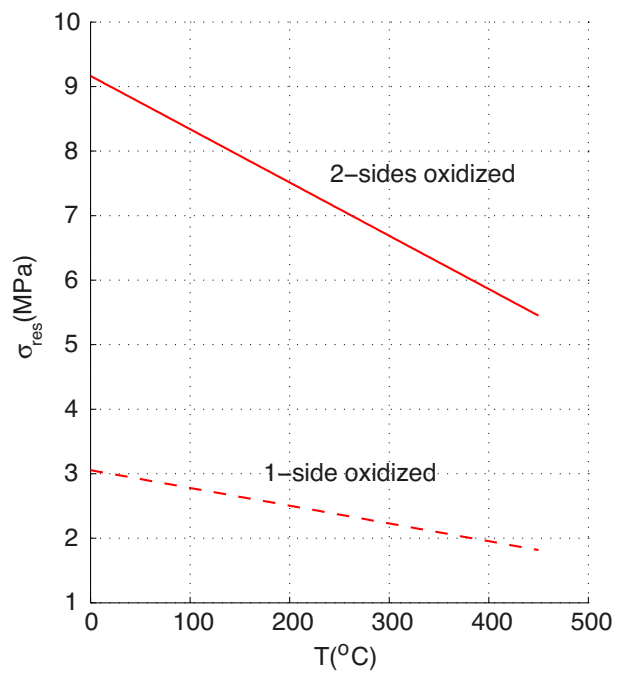


Figure 21: Evolution of residual stress associated to oxide layers with temperature.

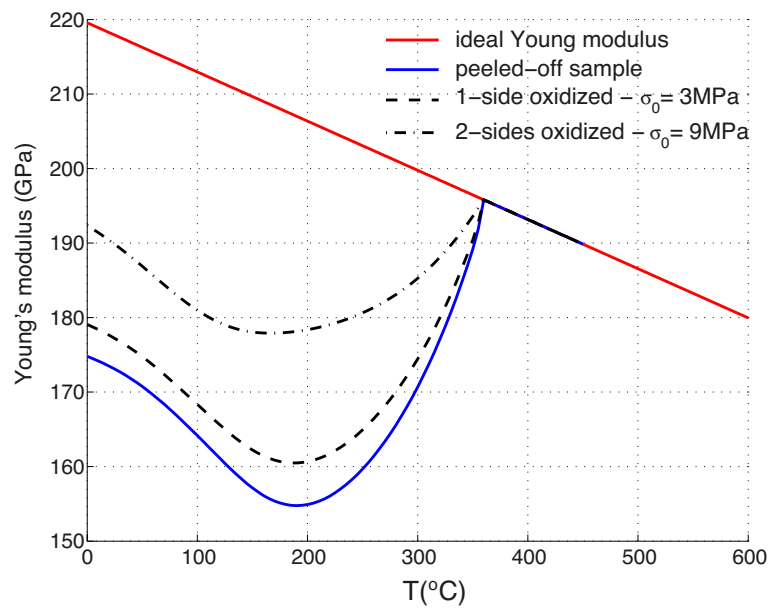


Figure 22: Influence of residual stress associated to oxide layers on the apparent nickel Young's modulus - homogeneous stress estimation.

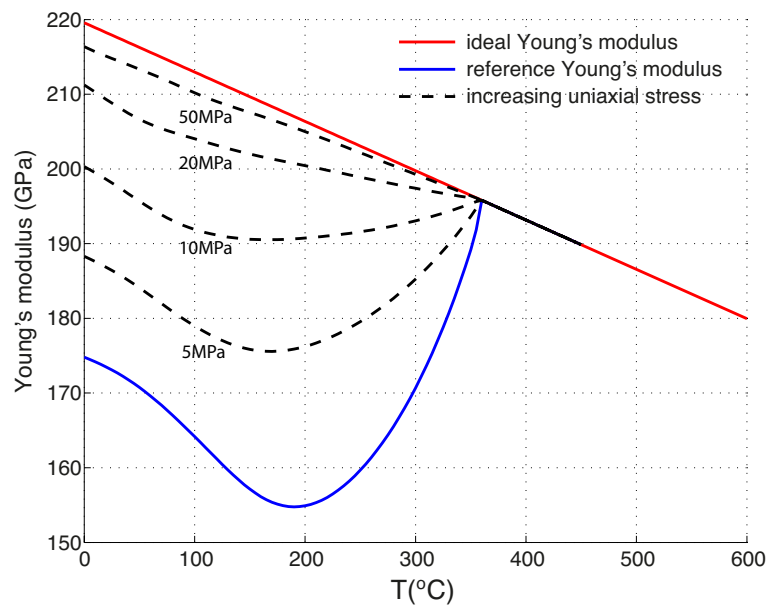


Figure 23: Change of nickel Young's modulus with temperature - effect of uniaxial applied stress - homogeneous stress estimation.

638 The model gives also the opportunity to test the influence of a magnetic  
 639 field on the apparent Young's modulus of nickel. The effect of a superim-  
 640 posed constant magnetic field  $H_3 = H_a$  is illustrated in figure 24.  $H_a$  varies  
 641 from 1000A/m to 10000A/m exhibiting the magnetic saturation phenomenon  
 642 already discussed in literature [6] and reported in figure 4a.

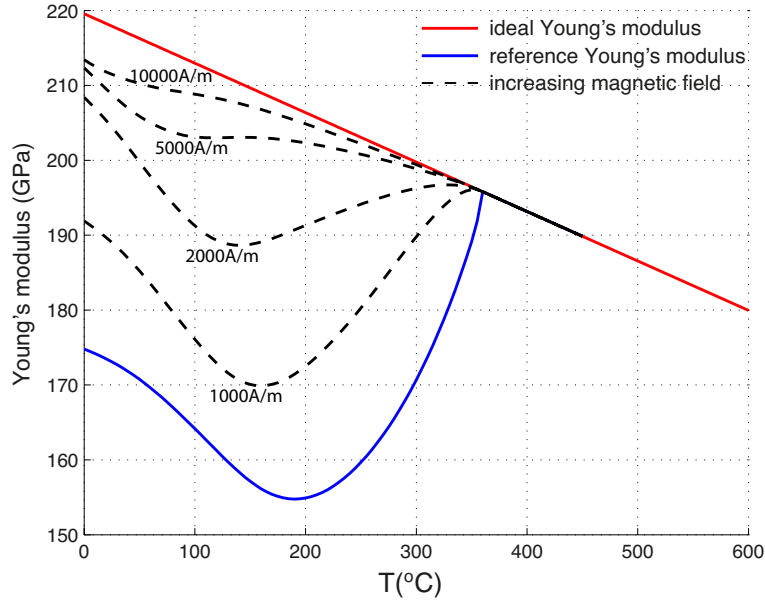


Figure 24: Change of nickel Young's modulus with temperature - effect of constant applied magnetic field - homogeneous stress estimation.

## 643 5. Conclusion

644 In this work a modeling of the variation of Young's modulus with temper-  
 645 ature of Ni and Ni-NiO layers has been proposed. The magnetic origin of this  
 646 behavior has first been underlined, justifying the use of a magneto mechanical  
 647 approach for the modeling. A first analytical modeling includes the change  
 648 of the saturation magnetization, of the initial anhysteretic susceptibility and  
 649 of the maximal magnetostriction with a relaxation of magneto-crystalline  
 650 anisotropy concomitant to increasing temperature. The second modeling is  
 651 a numerical modeling giving the average behavior of a representative volume  
 652 element composed of 546 regularly distributed grains. This modeling requires

653 to define the temperature dependence of many magnetic and magnetostric-  
654 tive parameters. It allows a continuous description of the change of Young's  
655 modulus with temperature.

656 The discrepancies observed with experiments concern the lower level of Young's  
657 modulus at room temperature up to 200°C (as observed for peeled-off, 1-side  
658 oxidized or 2-sides oxidized sample). Discrepancies can be explained mainly  
659 by the fact that the modeling is reversible although the physical phenomenon  
660 is irreversible (hysteresis effect) and that the variation of initial anhysteretic  
661 susceptibility with temperature remains unknown. Other uncertainties and  
662 approximations (infinite medium) are additive reasons.

663 It has also been shown that even if crystallographic texture remains roughly  
664 isotropic after oxidizing at 1100°C, the grain size increases drastically for  
665 high duration heat treatments [4]. This size may reach the thickness of the  
666 layer leading to a surface effect whose magnetic and magnetostrictive conse-  
667 quences have been extensively discussed in [36]. This surface effect may have  
668 important consequences on the global response of apparent elastic behavior  
669 because the domain structure is strongly modified by free surface conditions.  
670 The analysis proposed in this paper remains nevertheless sufficient to under-  
671 stand now clearly how the Ni-NiO system behaves. An extension to another  
672 *Ni / coating* system or more generally another *ferromagnetic substrate / coat-*  
673 *ing* system is possible, opening to a wide range of applications. It could be  
674 for example applied to the measurement of thickness deposits and/or to the  
675 inverse identification of internal stress levels inside a substrate.

## 676 **6. acknowledgements**

677 The authors wish to thank Jocelyne Balmain, LaSIE UMR 7356 CNRS,  
678 Université de La Rochelle, for her careful preparation of oxidized samples.

## 679 Appendix A. Multiscale modeling

680 The multiscale model involves three scales: domain scale, grain scale and  
681 polycrystalline scale (representative volume element -  $RVE$ ). It is especially  
682 dedicated to estimate the macroscopic magnetization and magnetostrictive  
683 responses to macroscopic magnetic field and/or stress loadings of polycrys-  
684 talline anisotropic media. Initially proposed by [26] at the grain scale, it was  
685 extended to polycrystals by [13] and [27]. In the present study, it is used to  
686 model the variation of magnetostriction with respect to stress ( $d\epsilon^u/d\sigma - \Delta E$   
687 effect) considering:

- 688 • free specimen (peeled-off sample)
- 689 • 1-side oxidized sample (biaxial stress -  $\sigma_0=3\text{MPa}$ )
- 690 • 2-sides oxidized sample (biaxial stress -  $\sigma_0=9\text{MPa}$ )
- 691 • increasing uniaxial stress on a sample
- 692 • increasing magnetic field on a sample

693 An isotropic grain distribution has been used. Since this model always  
694 refers to equilibrium, modeling results must be compared to anhysteretic  
695 (reversible) experimental measurements.

### 696 Appendix A.1. Micromagnetic model (grain scale)

697 A polycrystalline ferromagnetic media can be considered as an aggregate  
698 of single crystals assembled following the orientation data. The microscopic  
699 model proposed by [26] is written using the volumetric fraction  $f_\alpha$  of each  
700 domain family  $\alpha$  (six  $\langle 100 \rangle$  or height  $\langle 111 \rangle$  families depending on  
701 easy directions), and magnetization rotation (two angles  $\theta_\alpha$  and  $\phi_\alpha$  per do-  
702 main family) as internal variables. The potential energy (A.1) is defined for  
703 each magnetic domain family  $\alpha$  as the sum of the magneto-crystalline (A.2),  
704 magnetostatic (A.3) and elastic (A.4) energies, detailed hereafter.

$$W^\alpha = W_K^\alpha + W_H^\alpha + W_\sigma^\alpha \quad (\text{A.1})$$

$$W_K^\alpha = K_1(\gamma_1^2\gamma_2^2 + \gamma_2^2\gamma_3^2 + \gamma_3^2\gamma_1^2) + K_2(\gamma_1^2\gamma_2^2\gamma_3^2) \quad (\text{A.2})$$

$$W_H^\alpha = -\mu_0 \vec{H}^\alpha \cdot \vec{M}^\alpha \quad (\text{A.3})$$

$$W_\sigma^\alpha = \frac{1}{2} \boldsymbol{\sigma}^\alpha : \mathbb{C}^{\alpha-1} : \boldsymbol{\sigma}^\alpha \quad (\text{A.4})$$

705 where  $\vec{M}^\alpha = M_s \vec{\gamma}^\alpha$  is the magnetization vector of the domain family  $\alpha$   
 706 ( $M_s$ : saturation magnetization),  $\vec{\gamma}^\alpha$  denotes the direction of magnetization  
 707 ( $\gamma_i^\alpha$ : direction cosines) in the crystal frame.  $K_1$  and  $K_2$  are the magnetocrystal-  
 708 talline energy constants.  $\vec{H}^\alpha$  is the magnetic field at the domain scale.  $\boldsymbol{\sigma}^\alpha$   
 709 is the stress tensor at the domain scale.  $\mathbb{C}^\alpha$  denotes the stiffness tensor of a  
 710 domain family (or grain  $\mathbb{C}^g = \mathbb{C}^\alpha$ ). Homogeneous field and deformation as-  
 711 sumptions lead to a definition of magneto static and elastic energies involving  
 712 magnetic and mechanical loadings at the grain scale:

$$W_H^\alpha = -\mu_0 \vec{H}^g \cdot \vec{M}^\alpha \quad (\text{A.5})$$

$$W_\sigma^\alpha = -\boldsymbol{\sigma}^g : \boldsymbol{\epsilon}_\mu^\alpha \quad (\text{A.6})$$

713 where  $\boldsymbol{\epsilon}_\mu^\alpha$  denotes the magnetostriction strain tensor of a domain family  
 714  $\alpha$ , where  $\lambda_{100}$  and  $\lambda_{111}$  are the magneto-elastic constants:

$$\boldsymbol{\epsilon}_\mu^\alpha = \frac{3}{2} \begin{pmatrix} \lambda_{100}(\gamma_1^2 - \frac{1}{3}) & \lambda_{111}\gamma_1\gamma_2 & \lambda_{111}\gamma_1\gamma_3 \\ \lambda_{111}\gamma_1\gamma_2 & \lambda_{100}(\gamma_2^2 - \frac{1}{3}) & \lambda_{111}\gamma_2\gamma_3 \\ \lambda_{111}\gamma_1\gamma_3 & \lambda_{111}\gamma_2\gamma_3 & \lambda_{100}(\gamma_3^2 - \frac{1}{3}) \end{pmatrix}_{CF} \quad (\text{A.7})$$

715 At the grain scale, the volume fraction  $f_\alpha$  of a family domain  $\alpha$  is calcu-  
 716 lated using a statistical approach (Boltzmann function - A.8) [37] assuming  
 717 that a magnetic domain is much smaller than a representative volume element  
 718 (considered as a small body immersed into a large closed thermodynamic sys-  
 719 tem).  $\theta_\alpha$  and  $\phi_\alpha$  are the results of a minimization of the potential energy of  
 720 a domain family (A.10).

$$f_\alpha = \frac{\exp(-A_s \cdot W^\alpha)}{\sum_\alpha \exp(-A_s \cdot W^\alpha)} \quad (\text{A.8})$$

721 with

$$A_s = \frac{3\chi_0}{\mu_0 M_s^2} \quad (\text{A.9})$$

$$\{\theta_\alpha, \phi_\alpha\} = \min(W^\alpha) \quad (\text{A.10})$$

722  $\chi_0$ ,  $M_s$  and  $\mu_0$  are the initial anhysteretic susceptibility (model expressed  
 723 in reversible condition), the saturation magnetization and the vacuum permeability respectively. This formulation uses the assumption that initial  
 724 magnetization process is due to magnetic wall displacement and that rotation mechanism is neglected. This assumption is true for nickel at RT. An  
 725 increasing temperature may compromise this hypothesis (especially when  $K_1$   
 726 is reduced, that enhances the rotation mechanism).

729  $A_s$ , through its relation with  $\chi_0$ , is a parameter that accounts for energetic terms not considered in the final expression (exchange energy, magneto  
 730 static phenomena). Its expression evolves with temperature since saturation magnetization and initial anhysteretic susceptibility are temperature dependent.  
 731 Moreover, a global inverse proportionality dependence to temperature should be considered for  $A_s$  following the reference statistical approach [37],  
 732 leading to the final expression:  
 733  
 734  
 735

$$A_s = \frac{3\chi_0(T)}{\mu_0 M_s(T)^2} \frac{T^{RT}}{T} \quad (\text{A.11})$$

736 with  $T^{RT}$  the room temperature.

737

738 Assuming that the elastic behavior is homogeneous within a grain, the magnetostriction strain of a single crystal is written as the mean magnetostriction over the domains (A.12). The magnetization in a grain is defined as well (A.13).  
 739  
 740  
 741

$$\epsilon_\mu^g = \langle \epsilon_\mu^\alpha \rangle = \sum_\alpha f_\alpha \epsilon_\mu^\alpha \quad (\text{A.12})$$

$$\vec{M}^g = \langle \vec{M}^\alpha \rangle = \sum_\alpha f_\alpha \vec{M}^\alpha \quad (\text{A.13})$$

742 The discrete approach has been modernized by [27]. In this new version,  
 743 the easy directions are not defined *a priori*. The possible directions  $\vec{\gamma}^\alpha$  are  
 744 described through the mesh of a unit radius sphere ( $N$  unit vectors  $\vec{x}_n$ ). A

745 34635 points mesh has been used in the present study. This new approach  
 746 avoids the minimization operation A.10 and is less time consuming.

747 *Appendix A.2. Localization and homogenization*

748 Previous calculations are made for each grain of the polycrystalline ag-  
 749 gregate. The polycrystalline aggregate considered in the study is a regularly  
 750 distributed orientation data file made of 546 orientations [13]. The mag-  
 751 netic behavior at the polycrystalline scale is defined as the average value of  
 752 magnetization (A.14). A local demagnetizing field in each grain due to the  
 753 magnetization of the surrounding grains can be introduced [13, 36]: the mag-  
 754 netic field at the grain scale  $\vec{H}^g$  is defined as a function of the external field,  
 755 the mean secant equivalent susceptibility of the material  $\chi_m$ , ( $\chi_m = M/H$ )  
 756 and the difference between the mean magnetization  $\vec{M}$  and the magnetiza-  
 757 tion at the grain scale  $\vec{M}^g$  (A.15). The elastic behavior is obtained using  
 758 a self-consistent homogenization scheme. The macroscopic magnetostriction  
 759 strain (A.16) is estimated using the Eshelby's solution and considering the  
 760 local magnetostriction as a free strain;  $\mathbb{B}^g$  denotes the fourth order stress  
 761 concentration tensor.

$$\vec{M} = \langle \vec{M}^g \rangle \quad (\text{A.14})$$

$$\vec{H}^g = \vec{H} + \frac{1}{3 + 2\chi_m} (\vec{M} - \vec{M}^g) \quad (\text{A.15})$$

$$\epsilon_\mu = \langle {}^t \mathbb{B}^g : \epsilon_\mu^g \rangle \quad (\text{A.16})$$

762 The magnetostriction strain at the grain scale is elastically incompati-  
 763 ble and creates a stress that changes the magneto-elastic energy term (self-  
 764 stress). The stress at the grain scale  $\sigma^g$  is derived from the implicit equation  
 765 (A.17).

$$\sigma^g = \mathbb{B}^g : \sigma + \mathbb{C}^{acc} : (\epsilon_\mu - \epsilon_\mu^g) \quad (\text{A.17})$$

766 with the accommodation stiffness tensor:

$$\mathbb{C}^{acc} = ((\mathbb{C}^g)^{-1} + (\mathbb{C}^*)^{-1})^{-1} \quad (\text{A.18})$$

767 and the stress concentration tensor:

$$\mathbb{B}^g = \mathbb{C}^g : (\mathbb{C}^g + \mathbb{C}^\star)^{-1} : (\mathbb{C}^0 + \mathbb{C}^\star) : (\mathbb{C}^0)^{-1} \quad (\text{A.19})$$

768  $\mathbb{C}^\star = \mathbb{C}^0 : ((\mathbb{S}^{Esh})^{-1} - \mathbb{I})$  is the Hill's constraint tensor.  $\mathbb{C}^0$  is the stiffness  
 769 tensor of the effective medium. If a self-consistent scheme is chosen,  $\mathbb{C}^0$  refers  
 770 to the self-consistent stiffness tensor.  $\boldsymbol{\sigma}$  is the macroscopic stress.  $\mathbb{S}^{Esh}$  is the  
 771 so-called Eshelby tensor, calculated following Mura [35].

## 772 References

- 773 [1] N.P. Padture, M. Gell, E.H. Jordan, *Science* **296** (2002), pp. 280-284.
- 774 [2] X.Q. Cao, R. Vassen, D. Stoeber, *J. Eur. Ceram. Soc.* **24** (2004) pp.1-10.
- 775 [3] S.Guo, Y.Kagawa, *Scripta Materialia* **50** (2004), pp.1401-1406.
- 776 [4] M.Tatat, PhD Thesis, ENSMA, 2012.
- 777 [5] M. Tatat, P. Gadaud, P.-O. Renault, J. Balmain, C. Coupeau, X. Milhet,  
 778 *Mat. Sci. Eng. A*, **571** (2013) pp.92-94.
- 779 [6] Bozorth R.M., "Ferromagnetism", *ed. D. Van Norstand*, N.Y. 1951.
- 780 [7] Cullity B.D., "Introduction to magnetic materials", *ed. Addison-Wesley*,  
 781 N.Y. 1972.
- 782 [8] H. M. Ledbetter, R. P. Reed, *J. Phys. Chem. Ref. Data*, **2**, 3, (1973),  
 783 pp.531-617.
- 784 [9] S. Siegel, L. Quimby, *Phys. Rev.*, **49**, (1936) pp.663-670.
- 785 [10] A.M. Huntz, *Mater. Sci. Eng. A* **201** (1995) pp.211-228.
- 786 [11] O. Hubert, L.Daniel, *J. of Magn. and Magn. Mater.*, **323** (2011),  
 787 pp.1766-1781.
- 788 [12] L. Daniel, O. Hubert, *Eur. Phys. J. - Appl. Phys.*, **45** (2009) 31101.
- 789 [13] L. Daniel, O. Hubert, N. Buiron, R. Billardon. *J.of the Mech. and Phys.*  
 790 *of Solids*, **56** (2008), pp.1018-1042
- 791 [14] P. Gadaud, *Int. J. Mater. Prod. Technol.* **26** (2006), pp.238-326.

- 792 [15] ASTM E 1876-00, *Annual Book of ASTM Standards*, 03.01 (2001),  
793 pp.1099-1112.
- 794 [16] V. Hauk, "Structural and Residual Stress Analysis by Non-destructive  
795 Methods: Evaluation, Application, Assessment", ed. *Elsevier*, Amster-  
796 dam, The Netherlands, (1997).
- 797 [17] G. Simons and H. Wang, "Single Crystal Elastic Constants and Cal-  
798 culated Aggregate Properties: A HANDBOOK", second Edition, *The*  
799 *M.I.T. Press*, Cambridge, Massachusetts, and London, England, (1971).
- 800 [18] A. Aubry, F. Armanet, G. Beranger, J.L. Lebrun, G. Maeder, *Acta*  
801 *Metall.*, **36** (1988) pp.2779-2786.
- 802 [19] C. Liu, A.M. Huntz, J.L. Lebrun, *Mater. Sci. Eng. A* **160** (1993),  
803 pp.113-126.
- 804 [20] O. Hubert, R. Waberi, S. Lazreg, K. Huyn-Soo, R. Billardon, "Measure-  
805 ment and two-scales modeling of the  $\Delta E$  effect", in: 7th EUROMECH  
806 Solid Mechanics Conference, 2009.
- 807 [21] M. Bornert, T. Bretheau, P. Gilormini, "Homogenization in Mechanics  
808 of Material", ed. *Iste Publishing Company*, 2007.
- 809 [22] D. Kirkham, *Phys. Rev.* **52**, (1937), pp.1162-1167.
- 810 [23] E. Tatsumoto, T. Okamoto, Y. Kadana - *J. of the Physical Society of*  
811 *Japan*, **20** - Issue 8, (1965), pp. 1534-1534.
- 812 [24] E. Tatsumoto, T. Okamoto, N. Iwata, Y. Kadana, *J. of the Physical*  
813 *Society of Japan*, **20** - Issue 8, (1965), pp. 1541-1542.
- 814 [25] E. Ascher, *Helvetica Physica Acta*, **39** (1966), pp. 466-476.
- 815 [26] N. Buiron, L. Hirsinger, R. Billardon, *J. Phys. IV* **11** (2001) pp.373.
- 816 [27] N. Galopin, L. Daniel, *Eur. Phys. J. - Appl. Phys.*, **42** (2008) pp.153-159.
- 817 [28] C. Zener, *physical review*, **96**, num. 5, (1935), pp. 1335-1338.
- 818 [29] J. J. M. Franse, *Journal de Physique - C1* **32**, supplément au no 2-3,  
819 (1971), pp.186-192

- 820 [30] W.J. Carr, *J. appl. phys.*, **29** (1958), pp.436-437.
- 821 [31] S. Chikazumi, "Physics of Ferromagnetism", second ed., *Oxford Univer-*  
822 *sity Press*, 1997.
- 823 [32] E. Du Trémolet de Lacheisserie, D.Gignoux, M.Schlenker, " Magnetism-  
824 I", *Springer Science & Business Media*, 2005.
- 825 [33] H. Hauser, *J. Appl. Phys.*, **96** (5) (2004), pp. 2753-2767.
- 826 [34] L. Daniel, M. Rekik, O. Hubert, *Arch. of Appl. Mech.*: Volume 84, Issue  
827 9 (2014), pp.1307-1323.
- 828 [35] T. Mura, "Micromechanics of Defects in Solids", ed. *Martinus Nijhoff*  
829 *Publishers*, Dordrecht, MA, 1982.
- 830 [36] O. Hubert, L.Daniel, *J. of Magn. and Magn. Mater.*, **320** (2008),  
831 pp.1412-1422.
- 832 [37] A. Sommerfeld, "Thermodynamics and Statistical Physics", *Academic*  
833 *Press*, N.Y., 1955.